



## Article

# Mid-Deep Circulation in the Western South China Sea and the Impacts of the Central Depression Belt and Complex Topography

Hongtao Mai <sup>1,2</sup>, Dongxiao Wang <sup>1,2,\*</sup> , Hui Chen <sup>1,2,\*</sup>, Chunhua Qiu <sup>1,2</sup>, Hongzhou Xu <sup>2,3</sup>, Xuekun Shang <sup>1,2</sup> and Wenyan Zhang <sup>4</sup> 

<sup>1</sup> School of Marine Sciences, Sun Yat-sen University, Zhuhai 519082, China; maiht6@mail2.sysu.edu.cn (H.M.); qiuchh3@mail.sysu.edu.cn (C.Q.); shangxk@mail2.sysu.edu.cn (X.S.)

<sup>2</sup> Southern Marine Science and Engineering Guangdong Laboratory (Zhuhai), Zhuhai 519000, China; hzxu@idsse.ac.cn

<sup>3</sup> Institute of Deep-Sea Science and Engineering, Chinese Academy of Sciences, Sanya 572000, China

<sup>4</sup> Institute of Coastal Systems—Analysis and Modeling, Helmholtz-Zentrum Hereon, 21502 Geesthacht, Germany; wenyan.zhang@hereon.de

\* Correspondence: dxwang@mail.sysu.edu.cn (D.W.); chenhui27@mail.sysu.edu.cn (H.C.)

**Abstract:** As a key component of meridional overturning circulation, mid-deep circulation plays a crucial role in the vertical and meridional distribution of heat. However, due to a lack of observation data, current knowledge of the dynamics of mid-deep circulation currents moving through basin boundaries and complicated seabed topographies is severely limited. In this study, we combined oceanic observation data, bathymetric data, and numerical modeling of the northwest continental margin of the South China Sea to investigate (i) the main features of mid-deep circulation currents traveling through the central depression belt and (ii) how atmospheric-forcing (winds) mesoscale oceanic processes such as eddies and current–topography interactions modulate the mid-deep circulation patterns. Comprehensive results suggest that the convergence of different water masses and current–topography interactions take primary responsibility for the generation of instability and enhanced mixing within the central depression belt. By contrast, winds and mesoscale eddies have limited influence on the development of local circulation patterns at mid-deep depths (>400 m). This study emphasizes that the intensification and bifurcation of mid-deep circulation; specifically, those induced by a large depression belt morphology determine the local material cycle (temperature, salinity, etc.) and energy distribution. These findings provide insights for a better understanding of mid-deep circulation structures on the western boundary of ocean basins such as the South China Sea.

**Keywords:** mid-deep circulation; central depression belt; western boundary; South China Sea



**Citation:** Mai, H.; Wang, D.; Chen, H.; Qiu, C.; Xu, H.; Shang, X.; Zhang, W. Mid-Deep Circulation in the Western South China Sea and the Impacts of the Central Depression Belt and Complex Topography. *J. Mar. Sci. Eng.* **2024**, *12*, 700. <https://doi.org/10.3390/jmse12050700>

Academic Editor: Michael Lazar

Received: 25 February 2024

Revised: 18 April 2024

Accepted: 19 April 2024

Published: 24 April 2024



**Copyright:** © 2024 by the authors. Licensee MDPI, Basel, Switzerland. This article is an open access article distributed under the terms and conditions of the Creative Commons Attribution (CC BY) license (<https://creativecommons.org/licenses/by/4.0/>).

## 1. Introduction

Extensive research has demonstrated that continental slopes play a pivotal role in maintaining vorticity balance, facilitating energy cascades, promoting vertical mixing, and enabling cross-slope material exchange [1–8]. It is also widely acknowledged that continental slope morphology (such as slope orientation [9] and steepness [10]) is able to significantly regulate the mid-deep circulation pattern, especially well known as the western boundary intensification [11].

The seabed morphology on continental margins, including western and eastern boundaries, is diverse and exhibits intricate topographic features [12,13], including seamounts (raised), canyons (concave), terraces (wide), etc. Understanding how these topographic changes interact with multi-scale oceanic processes and, consequently, affect the structure and dynamics of mid-deep circulations has attracted considerable attention [14–17]. However, the scarcity of observational data has seriously impeded the advancement of our understanding [18].

Based on Conductivity–Temperature–Depth (CTD) and Lowered Acoustic Doppler Current Profiler (LADCP) observation conducted during the summer of 2022, and combined with bathymetric data and numerical simulation results of the Hybrid Coordinate Ocean Model (HYCOM), we confirm the summer circulation pattern and reveal the relationship between mid-deep circulation evolution and topography in the central depression belt.

This study investigates the mid-deep circulation dynamics when currents pass through a large depression (with a total length exceeding 500 km, named the central depression belt) along the northwest continental margin of the South China Sea (SCS) (Figure 1). We also explore how winds, eddies, and current–topography interactions modulate the local circulation. Our study reveals that the SCS mid-deep currents running through the central depression belt are evidently reinforcing and branching where diverse water masses coexist and interact with each other. Through the large depression belt, the degree of their mixing varies spatially and is closely related to current–topography interaction. These findings emphasize that, when passing through basin boundaries with complex seabed topographies (such as a larger depression at a scale up to hundreds of km), topographic effects are decisive for developing local mid-deep circulation patterns and associated energy cascades.

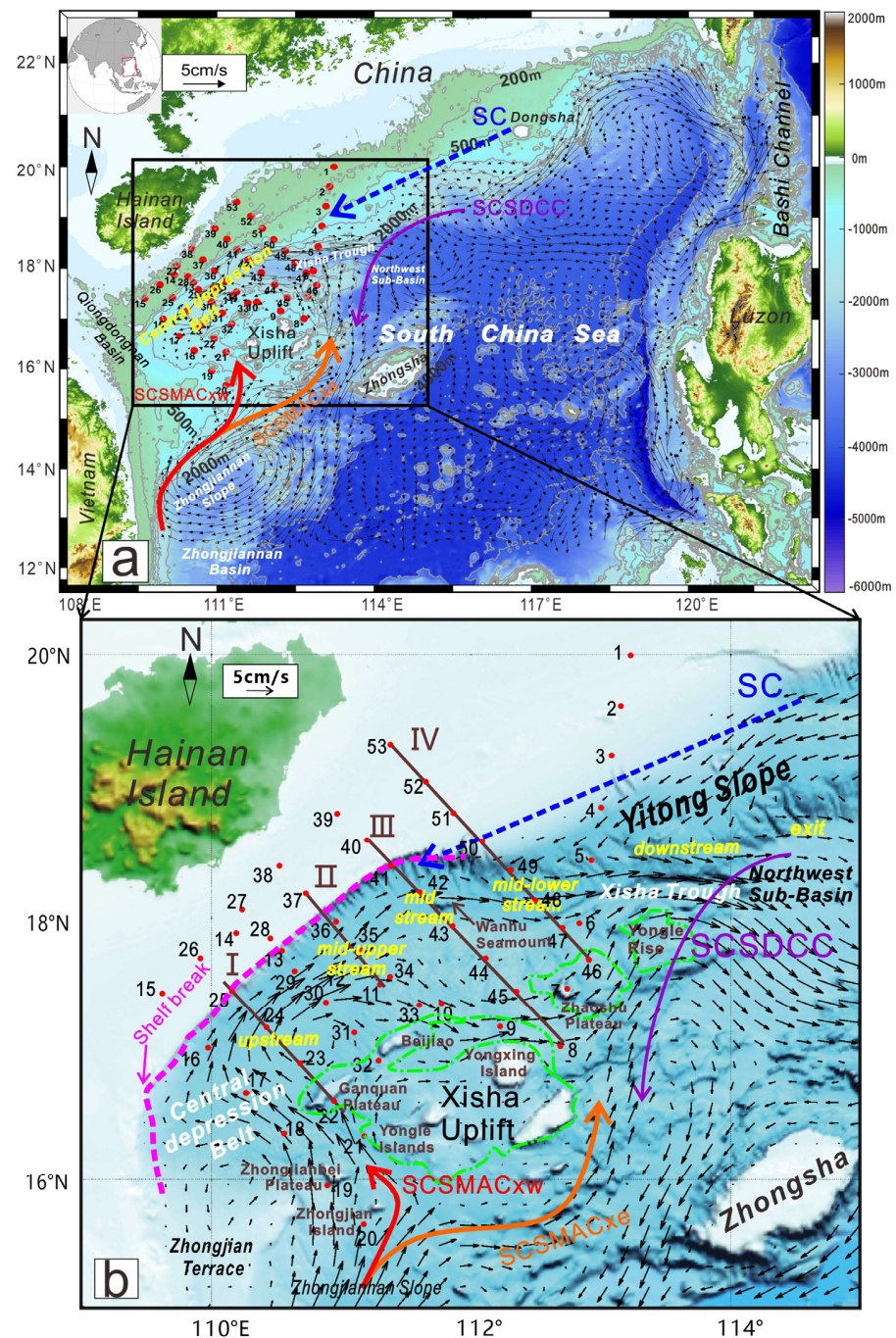


**Figure 1.** (a) Bathymetry of the northern South China Sea (SCS) margin derived from General Bathymetric Chart of the Oceans (GEBCO). Red dots represent the locations of observation stations (CTD and LADCP). The black vectors represent climatological summer (May–June–July/MJJ) currents at 1000 m depth derived from HYCOM GLBu0.08. The orange arrow is the eastern branch of the middle-layer anticyclonic circulation of SCS (SCSMAC) in the Xisha (SCSMACxe). The red arrow is the western branch of SCSMAC in the Xisha (SCSMACxw), data from [19]. The blue dashed arrow is the slope current (SC), data from [20,21]. The purple arrow is the deep-layer cyclonic circulation of SCS (SCSDCC), data from [22–25]. (b) Topographic map from Atlas of Geology and Geophysics of the SCS (1:2,000,000), with its location shown in a black box (a). The black vectors represent the MJJ depth-averaged currents in the Xisha region (400–1300 m), derived from the HYCOM result. The arrows represent currents that are the same as (a). The green dashed lines are uplift areas. The magenta dashed line is the shelf break. The brown lines represent the locations of selected sections showing seabed morphologies in Figures 2 and 3, including the upstream, the mid-upper stream, the midstream, and the mid-lower stream.



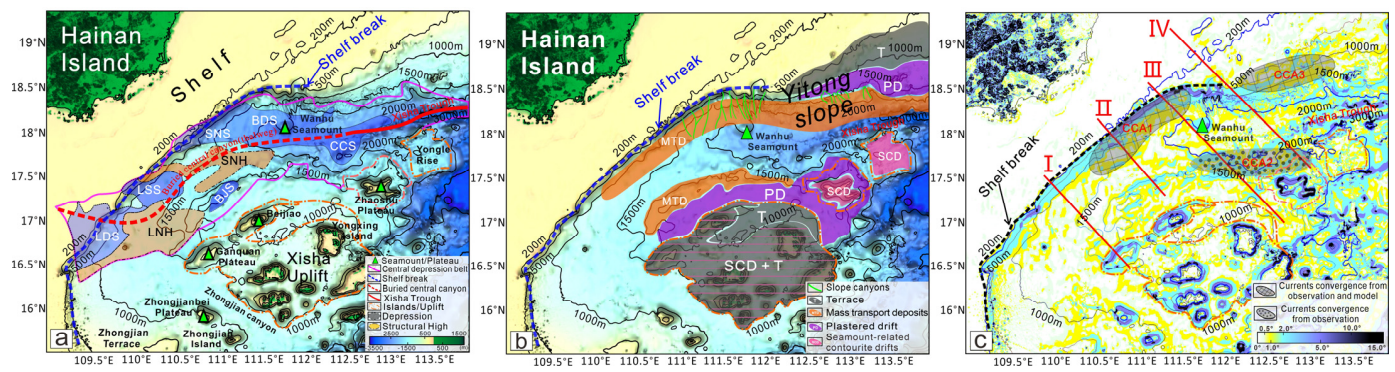


**Figure 2.** Map of structural zone (a), geomorphology (b), and slope (c) in the central depression belt derived from GEBCO. The orange dashed lines: uplift areas. In (a), YBS: Yabei Sag; SXS: Songxi Sag; SDS: Songdong Sag; High. LDS: Ledong Sag; LNH: Lingnan High; LSS: Lingshui Sag; BJS: Beijiao Sag; SNH: Songnan High; SNS: Songnan Sag; BDS: Baodao Sag; CCS: Changchang Sag. In (c), CCA 1, 2, and 3: currents convergence areas.

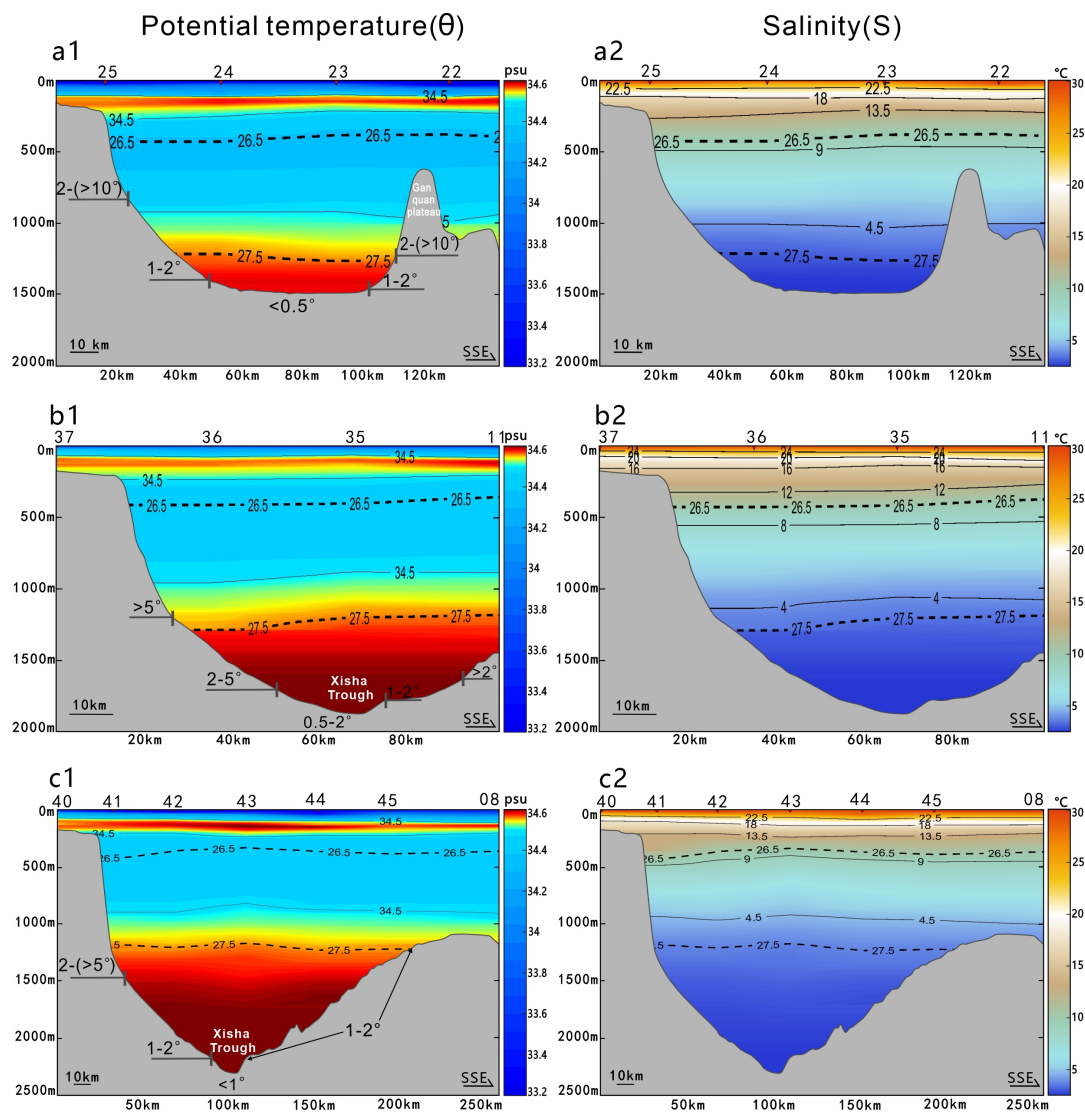


**Figure 3.** Cont.



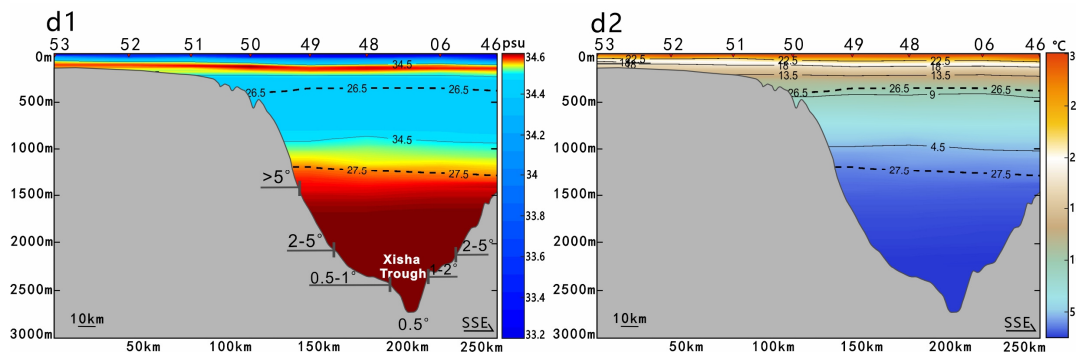


**Figure 3.** Potential temperature ( $\theta$ ), salinity ( $S$ ), and topography features on multiple profiles through the central depression belt. (a) Profile (I) with stations 25-22 (from NW to SE) in the upstream depression belt ((a1) =  $\theta$ , (a2) =  $S$ ). (b) Profile (II) with stations 37-11 in the mid-upper stream depression belt ((b1) =  $\theta$ , (b2) =  $S$ ). (c) Profile (III) with stations 40-08 in the midstream depression belt ((c1) =  $\theta$ , (c2) =  $S$ ). (d) Profile (IV) with stations 53-46 in the mid-lower stream depression belt ((d1) =  $\theta$ , (d2) =  $S$ ). The thick black dashed line represents the potential density ( $\sigma_\theta$ ) = 26.5–27.5 kg·m<sup>-3</sup>.

## 2. Data and Methods

### 2.1. Observation Data

Direct measurements of temperature, salinity, pressure, and sound velocity were conducted while on a cruise of the R/V Zhong Shan Da Xue from 22 June to 7 July 2022. Across the central depression belt and continental slope, a total of 53 stations were placed spanning over four regions (Figure 1b) from southwest to northeast: stations 15-26 in the upstream depression belt; stations 09-14, and 27-38 in the mid-upper stream; stations 07, 08, and 39-45 in the midstream; stations 01-06 and 46-53 in the mid-lower stream. To derive a comprehensive structure of the mid-deep circulation (>400 m) in this depression belt, we selected four cross-sections (NW–SE aligned) for description in detail: the upstream profile (I) with stations 25-22, the mid-upper stream profile (II) with stations 37-11, the midstream profile (III) with stations 40-08, and the mid-lower stream profile (IV) with stations 53-46 (note that there are no velocity data for station 47, thus, station 06 is used instead) (Figure 1b).

The SBE 911plus CTD (24 Hz; Sea-Bird Scientific, Bellevue, WA, USA) and RDI Workhorse LADCP (300 kHz; Teledyne Marine, Daytona Beach, FL, USA) systems were installed on the CTD frame and simultaneously lowered. The CTD system provided precise measurements of potential temperature, conductivity, and pressure, with an accuracy of 0.0002 °C, 0.00004 S/m, and 0.001% FS, respectively. The CTD data were processed according to standard procedures and bin averaged to 1 m resolution. Most CTD measurements can reach 50 m above the bottom. The LADCP system was equipped with a dual-frequency system, incorporating both 300 kHz downward- and upward-looking acoustic beam profilers. The vertical bin size of the LADCP was 10 m, and there were 20 bins for each LADCP. In conjunction with the CTD, shipborne GPS, and LADCP bottom tracking, LADCP data processing was conducted using standard LADCP LDEO software version IX\_14 ([https://www.ldeo.columbia.edu/cgi-bin/ladcp-cgi-bin/hgweb.cgi/LDEO\\_IX](https://www.ldeo.columbia.edu/cgi-bin/ladcp-cgi-bin/hgweb.cgi/LDEO_IX), accessed on 24 February 2022) [26].

Since the investigated depression belt is oriented SW–NE (Figure 1b), LADCP and tidal velocities were transformed into a custom coordinate system (counterclockwise rotation) to calculate the velocity component parallel to the central depression belt, with the x-axis along with the main depression belt's elongation and the y-axis across cutting:

$$U(Z_h, t_i) = [u(Z_h, t_i) - u_{tide}(t_i)]\cos(\alpha) + [v(Z_h, t_i) - v_{tide}(t_i)]\sin(\alpha) \quad (1)$$

Here,  $u(Z_h, t_i)$  and  $v(Z_h, t_i)$  represent LADCP velocity components at various depths ( $h = 10$  m, 20 m, 30 m, ...) for each station ( $i = 1, 2, 3 \dots 53$ ). Similarly,  $u_{tide}(t_i)$  and  $v_{tide}(t_i)$  denote the zonal and meridional tidal velocity components at the closest time of LADCP for each station ( $i = 1, 2, 3 \dots 53$ ), respectively. The tidal velocity component was

calculated using the TPXO9 model (<https://www.tpxo.net/global/tpxo9-atlas>, accessed on 24 February 2022) [27], employing the harmonic constants of the four major tides O1, K1, M2, and S2 as boundary forcing from 20 June to 10 July 2022, with a 5 min resolution. The angle of the counterclockwise rotation was set as  $\alpha = 45^\circ$ .  $U(Z_h, t_i)$  was adjusted by subtracting the tidal velocities based on the TPXO9 model.

## 2.2. HYCOM Simulation

HYCOM (Hybrid Coordinate Ocean Model) is a numerical ocean circulation model that combines primitive equations of motion with hybrid vertical coordinates. It utilizes a hybrid vertical coordinate system that smoothly transitions from terrain-following coordinates. The numerical model data used in this study were derived from the HYCOM GLBu0.08 (<https://www.hycom.org/dataserver/gofs-3pt0/reanalysis>, accessed on 24 February 2022), which assimilated the satellite altimeter and sea surface temperature data together with available temperature and salinity profiles from Expendable Bathythermographs (XBTs), ARGO floats, and moored buoys [28]. The HYCOM GLBu0.08 offered a spatial resolution of approximately 10 km, which was specifically designed to capture circulation and eddy variability.

In the vertical plane, HYCOM GLBu0.08 interpolated the temperature, salinity, and velocity data to 40 levels. The climatological summer (MJJ) applied in this study used the 20-year average from May–July of 1993–2012.

## 2.3. Bathymetric Data

The General Bathymetric Chart of the Oceans (GEBCO) released the GEBCO\_2023, a continuous global terrain model for ocean and land with a spatial resolution of 15 arc seconds (~0.5 km). This dataset is a fusion of land topography with measured and estimated seafloor topography and was derived from a website (<https://www.gebco.net>, accessed on 24 February 2022).

## 2.4. Richardson Number and Fine-Scale Parameterization

The degree of shear stress is applied to evaluate the flow stability. The Richardson number ( $Ri$ ) space is used as a criterion:

$$Ri = \frac{N^2}{S^2}, \quad (2)$$

The velocity shear variance  $S^2 = (\partial U / \partial z)^2 + (\partial V / \partial z)^2$  was calculated with  $\partial z = 10$  m, where  $U$  and  $V$  represent the east–west components of the horizontal flow obtained from the LADCP, respectively.  $N^2 = -(g/\rho)\partial\rho/\partial z$ ,  $N$  is the buoyancy frequency, with  $g$  denoting the gravity acceleration and  $\rho$  representing the fluid density. When  $Ri < 0.25$ , mixing occurs due to shear; when  $Ri > 0.25$ , stratification suppresses mixing [29,30].

Fine-scale parameterizations to estimate the intensity and spatial distribution of turbulent diapycnal mixing in the ocean. The MacKinnon-Gregg model ( $\varepsilon_{MG}$ ) can be expressed in terms of fine-scale shear and stratification as [31]:

$$\varepsilon_{MG} = \varepsilon_0 \left( \frac{N}{N_0} \right) \left( \frac{S}{S_0} \right), \quad (3)$$

where  $S_0 = N_0 = 5.1 \times 10^{-3} \text{ rad s}^{-1}$  and  $\varepsilon_0$  is a background constant that adjusts the parameterized dissipation rate to the observational data.  $\varepsilon_0$  can vary significantly across different regions, typically ranging from  $10^{-10}$  to  $10^{-8} \text{ W/kg}$ . In this study, we choose  $\varepsilon_0 = 2.5 \times 10^{-9} \text{ W/kg}$  [32–34]. The  $\varepsilon_{MG}$  was estimated with the 10 m shear and buoyancy frequency; thus,  $\varepsilon_{MG}$  has a vertical resolution of 10 m. Diapycnal diffusivity ( $K_\rho$ ) was estimated by following the Osborn [35] formula  $K_\rho = \varepsilon/\Gamma$ , where  $\Gamma$  is the mixing efficiency, and  $\Gamma = 0.2$  is typically adopted [36]. The estimated  $\varepsilon_{MG}$  and  $K_\rho$  values affected by the surface mixed layers (above 50 m) were excluded from the parameterizations.

### 3. Results

#### 3.1. Geomorphology

In the Qiongdongnan Basin, the central depression belt contains the buried central canyon in the west and the Xisha Trough in the east [37], which extends over 500 km paralleling the regional slope/shelf break extension (in the SW–NE direction). It has concave-down widths ranging from 50 to 150 km, accompanied by secondary depressions and lower uplifts. From the southwestern upstream to the Xisha Trough, its average bottom depth increases from 1000 m to >3000 m (Figures 1 and 2).

There are four regions in this depression belt from SW to NE: upstream, midstream (containing the Wanhua Seamount as a marker), downstream, and the exit (Figure 1a). Upstream is represented by profile (I), mid-upper stream by profile (II), mid-stream by profile (III), and mid-lower stream by profile (IV). The Wanhua Seamount occupies an area of around  $20 \times 10 \text{ km}^2$  and stands ~500 m higher than the surrounding, representing the middle inflection point of the S-shaped central depression belt (Figures 1 and 2a). The depression has a wider upstream (the distance between isobaths of 1000 m on the NW and SE flanks is ~100 km). It narrows in the midstream (~50–80 km) and widens again downstream (~150 km) (Figure 3).

Mass-wasting deposits (submarine landslides) and a number of slope-confined canyons develop on the NW slopes of the central depression belt (Figure 2b) [37–39]. They lie below the shelf break in the upstream and middle streams and have a deeper depth of over 1500 m downstream, where the average slope gradient is over  $2^\circ$  (locally over  $5^\circ$ ). The latter case contains plastered drifts and terraces that are located at shallower depths at 1000–1500 m ( $\sim 1^\circ$  to  $2^\circ$  of slope) and 500 to 1000 m ( $\sim 0.5^\circ$  to  $1^\circ$  of slope), respectively (Figure 2b) [40].

A relatively gentle slope ( $\sim 1^\circ$  to  $2^\circ$  in general, over  $2^\circ$  locally) characterizes the SE flank of the central depression belt (Figure 2c), and it connects to the uplift zones to the east, such as the Xisha Uplift and Yongle Rise (Figure 2a), where multiple obstacle/seamount-related contourite drifts develop among the uplift area above 1000 m depth [41] (Figure 2b). Local mass-wasting deposits are reported in the upstream at ~1200–1500 m [37] and the rest slopes are known as plastered drifts [41–43].

In profile (I), this depression's concave spans ~100 km in width, with a flat (slope  $< 0.5^\circ$ ) bottom at ~1500 m in depth. Both the NW and SE sides of depression belt walls, at depths from ~750 to ~250 m and ~2250 to ~600 m, respectively, exhibit steep slopes from  $2^\circ$  to over  $10^\circ$ , where the SE side refers to the Ganquan Plateau (Figure 3(a1)).

In profile (II), this depression spans ~50–80 km in width and has its thalweg depth at ~1900 m, and the base region is  $0.5^\circ$ – $1^\circ$  of slope. The vast majority of its NW flank presents slope gradients of  $>2^\circ$  (~1700 to ~1200 m deep), where even steeper slopes ( $>5^\circ$ ) dominate depths above ~1200 to ~250 m. The overall SE flank, in comparison, has gentle slope gradients between  $1^\circ$  and  $2^\circ$ , with slopes greater than  $2^\circ$  recognized in local undulations (e.g., obstacles or hills). (Figure 3(b1)).

In profile (III), this depression spans ~180 km in width and has its thalweg depth at ~2300 m, where the slope is less than  $1^\circ$ . Its NW flank presents slope gradients of  $>1^\circ$ , where steeper slopes ( $2^\circ$  to  $>5^\circ$ ) dominate depths of ~1500 to ~250 m. The overall SE flank, again, has gentle slope gradients of  $1^\circ$ – $2^\circ$ , with slopes greater than  $2^\circ$  occurring only in local undulations (Figure 3(c1)).

After entering the lower part of this depression (on the east side), ~150 km in width, the NW side mainly presents slopes between  $2^\circ$  and  $5^\circ$ . Profile (IV) stands at the mid-lower stream, where the apparent concavity at the bottom corresponds to the Xisha Trough (with a flat base of  $0.5^\circ$  at ~2700 m deep, ~7 km wide; the slopes on both sides are  $2^\circ$  to  $>5^\circ$ ). The depression's NW flank consists of three levels: the ~2200 to 2500 m terrace has slopes between  $0.5^\circ$  and  $1^\circ$ ; the ~2100 to 1500 m slope is  $2^\circ$ – $5^\circ$ ; even steeper slopes of  $>5^\circ$  dominate depths of ~1500 to 500 m. The SE flank contains two levels: the ~2300 to 2200 m terrace has slopes between  $1^\circ$  to  $2^\circ$ ; the ~2200 to 1500 m is generally  $2^\circ$ – $5^\circ$ , which belongs to the northeast foothill of the Zhaoshu Plateau (Figure 3(d1)).



### 3.2. Ocean Dynamics

#### 3.2.1. Water Masses

The blue dots of the CTD observation data in the Potential temperature ( $\theta$ )—Salinity (S) diagram show a vertically inverted S shape. Their tendency is consistent with that of the western SCS water mass (red curve) but deviates from the western Pacific water mass (black curve) (Figure 4a).

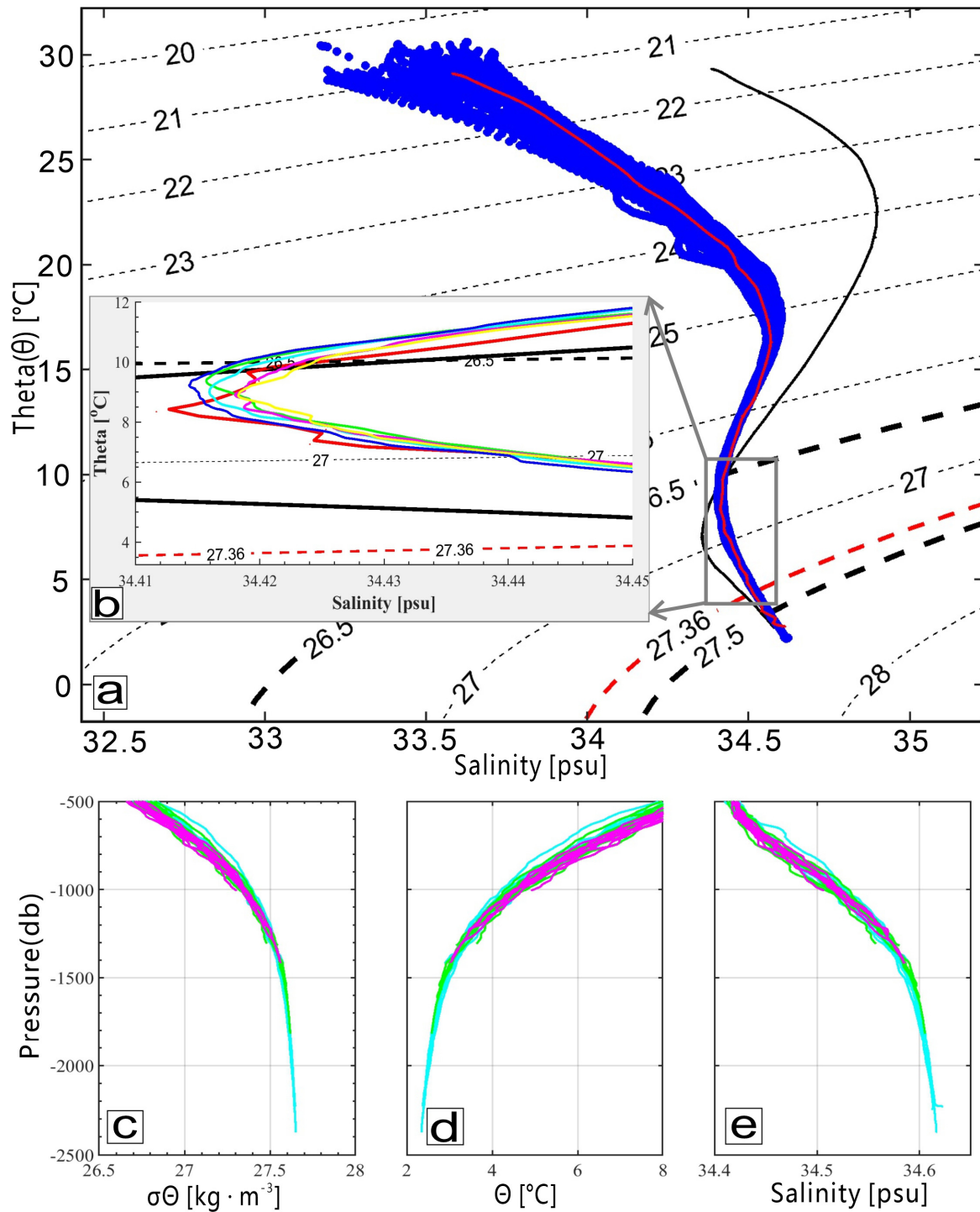


**Figure 4.** Potential temperature–salinity ( $\theta$ –S) diagram. (a) The black curve represents the average  $\theta$ –S profile of the Western Pacific, and the red curve corresponds to that of the Western South China Sea (obtained from WOA18, <https://www.ncei.noaa.gov/products/world-ocean-atlas>, accessed on

24 February 2022). The blue dots represent observation data in this study. The thick black dashed line represents  $\sigma\theta = 26.5\text{--}27.5 \text{ kg}\cdot\text{m}^{-3}$ . The red dashed line ( $\sigma\theta = 27.36 \text{ kg}\cdot\text{m}^{-3}$ ) represents depth = 1000 m. (b) Average  $\theta$ – $S$  diagram over the central depression belt. The yellow curve, magenta curve, green curve, blue curve, and cyan curve indicate regions of the NW flank of the upstream, the SE flank of the upstream, at the mid-upper stream, the NW flank of the midstream to mid-lower stream, and the SE flank of the midstream to mid-lower stream, respectively. (c)  $\sigma\theta$ –depth diagram. (d)  $\theta$ –depth diagram. (e) Salinity–depth diagram. In (c–e), the magenta, green, and cyan represent data from the upstream, the mid-upper stream, and the midstream to mid-lower stream.

The SCS Intermediate Water (SIW) layer is defined as having the potential density ( $\sigma\theta$ ) of  $26.5\text{--}27.5 \text{ kg}\cdot\text{m}^{-3}$  with a pressure of 0 dbar (occupying  $\sim 500\text{--}1500$  m deep in the Luzon Strait) [19,41,42] and corresponds to a depth range of  $\sim 400\text{--}1300$  m in the central depression belt region. Within this scope, a  $\sim 600\text{--}700$  m thick layer presents low average salinity ( $<34.5$  psu), where  $\theta$  ranges between 4 and  $11^\circ\text{C}$  (Figure 3). A distinct low-salinity peak ( $\sim 34.41$  to  $34.42$  psu) occurs where  $\theta$  is  $\sim 9^\circ\text{C}$ . In Figure 4b, the yellow curve corresponds to data at the NW side of the upstream central depression belt, with salinity of  $\sim 34.42$  psu at the highest peak; the blue curve represents the NW side of the mid-lower stream depression belt, with salinity of  $\sim 34.41$  psu at the lowest peak.

The SCS Deep Water (SDW) layer had a  $\sigma\theta$  of  $27.5 \text{ kg}\cdot\text{m}^{-3}$  (over 1500 m deep in the Luzon Strait) [19,44,45] and corresponds to depths of  $>1300$  m in the central depression belt region. In this scope,  $\theta$  decreases to  $<5^\circ\text{C}$ , and salinity increases to  $>34.5$  psu. Such a low-temperature, high-salinity property in the central depression belt deep water layer closely resembles that of the West Pacific water mass (Figure 4a).

### 3.2.2. Observational Currents Properties in the Central Depression Belt

Extending from the upstream central depression belt towards the NE, local currents (e.g., (i) the western branch of middle-layer anticyclonic circulation of SCS in the Xisha (SCSMACxw); (ii) the western branch of SCSMACxw in the mid-upper stream depression belt (SCSMACxw1); (iii) the eastern branch of SCSMACxw in the mid-upper stream depression belt (SCSMACxw2); (iv) the reversed branch of SCSMACxw in the upper-midstream depression belt (SCSMACxw3); (v) the middle-layer anticyclonic circulation of SCS in the Yitong slope (SCSMACy); (vi) the slope current (SC); (vii) the upper-layer western branch of deep-layer cyclonic circulation of SCS in the Xisha (SCSDCCxw); (viii) the lower-layer western branch of deep-layer cyclonic circulation of SCS in the Xisha (SCSDCCxlw); (ix) the eddy-induced current (EC) is identified in the horizontal and vertical distributions (Figure 5(a1,b1) and 6(a1,b1,c1,d1)). Their detailed features are listed (see Supplementary Table S2).

SCSMACxw flowing northeastward is recognized at station 24 in profile (I) and has a velocity of  $>10\text{--}20$  cm/s at a depth of  $300\text{--}1100$  m ( $\sim 40$  km wide), with a positive  $\theta$  anomaly of  $>+0.4^\circ\text{C}$  (Figures 6(a1) and 7(a2)). Profile (II) shows that it bifurcates into two branches of SCSMACxw1 and SCSMACxw2 (Figure 6(b1)). Regarding station 22, in profile (I), SCSMACxw reverses and flows southwestward, developing as SCSMACxw3, with velocities  $<10$  cm/s and a positive  $\theta$  anomaly (Figures 6(a1) and 7(a2)).

Passing station 36 in profile (II), SCSMACxw1 has a smaller velocity of  $<20$  cm/s ( $\sim 30$  km wide) and thickness than those of SCSMACxw in profile (I) (Figure 6(b1)). It continues progressing northeastward and passing through station 41 in profile (III) and station 50 in profile (IV), with velocities reducing to  $<10$  cm/s ( $\sim 10$  km wide) (Figure 6(c1,d1)). Synchronously, the  $\theta$  anomaly of the upper SCSMACxw1 is  $>+0.4^\circ\text{C}$  at depths of  $300\text{--}500$  m, and its width gradually narrows from  $\sim 60$  km in profile (II) to  $\sim 30$  km in profile (III) and to  $\sim 10$  km in profile (IV). Below 500 m, the  $\theta$  anomaly of the lower SCSMACxw1 decreases from  $<+0.4^\circ\text{C}$  in profile (II) to  $-0.2$  to  $+0.2^\circ\text{C}$  in profile (III) (Figure 7(b2,c2,d2)).

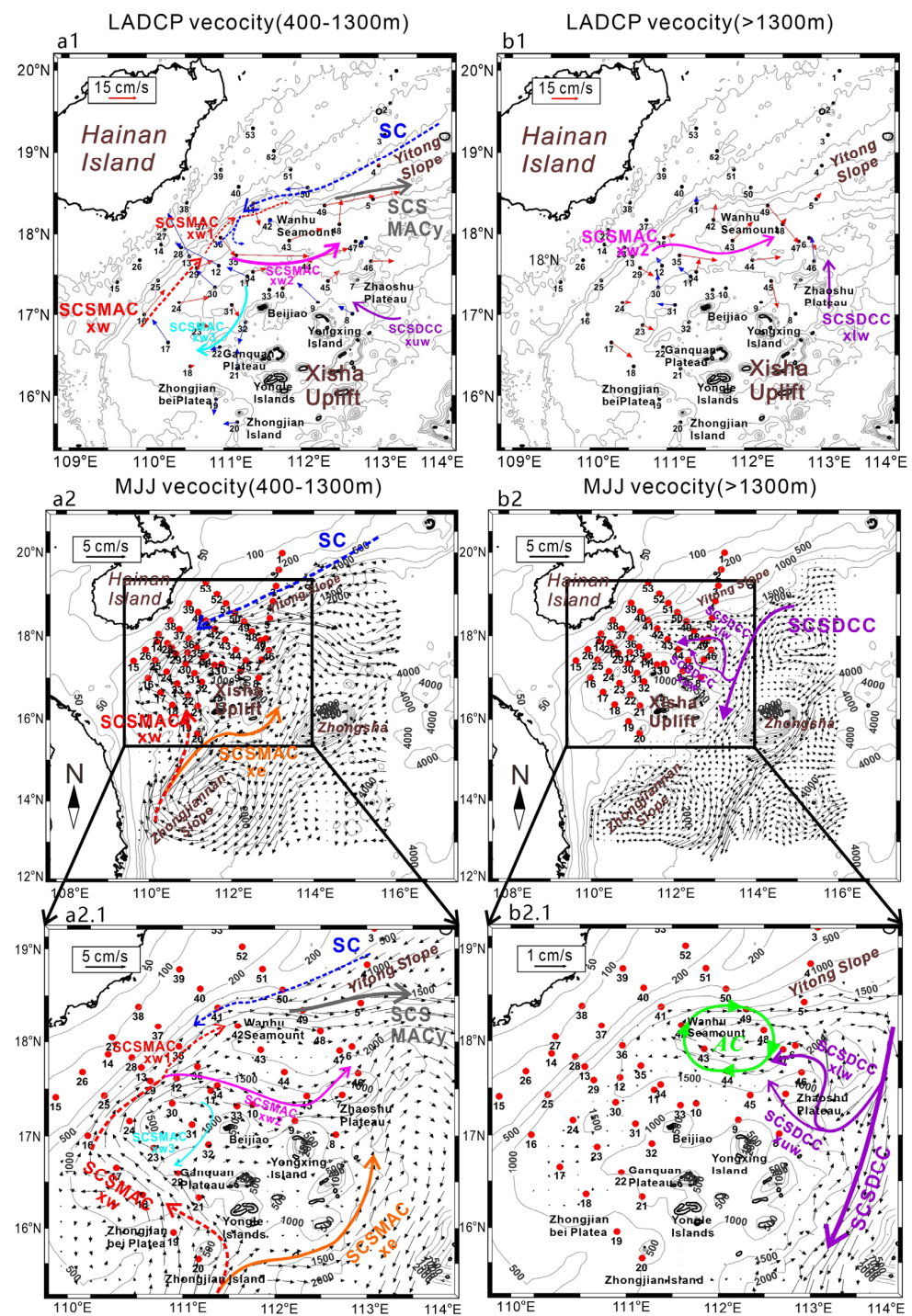


**Figure 5.** (a) Depth-averaged velocity distribution for the middle layer (400–1300 m) in the central depression belt. Orange arrows = SCSMACxe; red dashed arrows = SCSMACxw and SCSMACxw1; magenta arrows = SCSMACxw2; cyan arrow = SCSMACxw3; gray arrows = SCSMACy; blue dashed arrows = SC; purple arrows = SCSDCCxuw. (a1) LADCP velocity from various stations. The red vectors represent the eastward component, while the blue vectors correspond to the westward component. Bathymetry derived from GEBCO\_2023 (~0.5 km). (a2) Climatological summer (MJJ) velocity from HYCOM results. Bathymetry derived from HYCOM GLBu0.08 (~10 km). (a2.1) The local zoom is shown in the black box in (a2). (b) Depth-averaged velocity distribution for the deep layer (below 1300 m). Magenta arrows = SCSMACxw2; purple arrows = SCSDCC, SCSDCCxuw, and SCSDCCxlw; green arrows = local anticyclonic circulation. (b1) LADCP velocity. (b2) Climatological summer (MJJ) velocity from HYCOM results. (b2.1) The local zoom is shown in the black box in (b2).



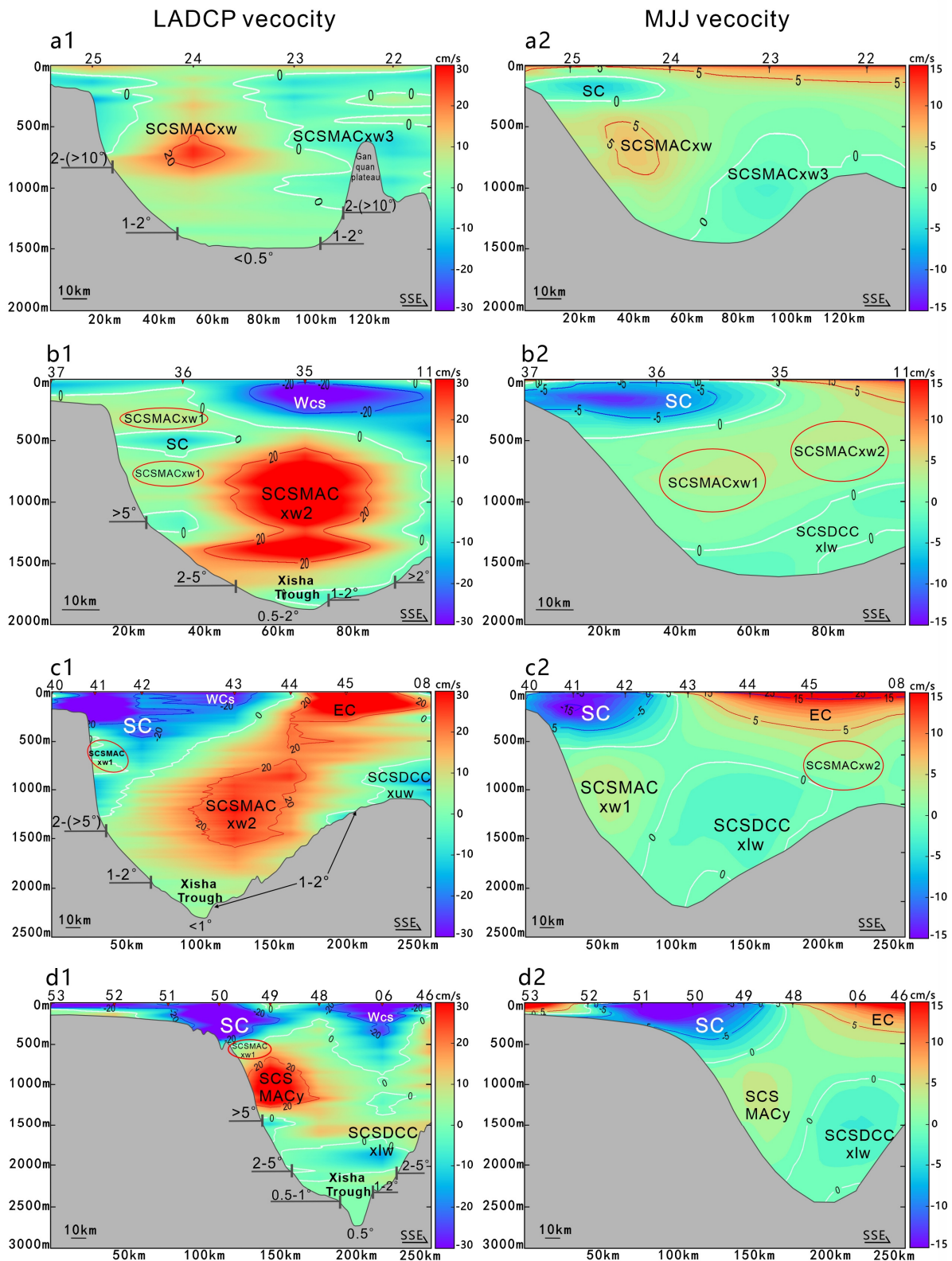


**Figure 6.** Profiles showing vertical velocity components ( $U$ ) (positive/red: flowing northeast, negative/blue: flowing southwest) and seabed morphologies (LADCP velocity with a high-resolution bathymetry ( $\sim 0.5$  km); MJJ velocity with a low-resolution bathymetry ( $\sim 10$  km)). (a1,b1,c1,d1) LADCP velocity in the upstream, mid-upper stream, midstream, and mid-lower stream depression belt, respectively. (a2,b2,c2,d2) Climatological summer (MJJ) velocity from HYCOM results in the upstream, mid-upper stream, midstream, and mid-lower stream depression belt, respectively.

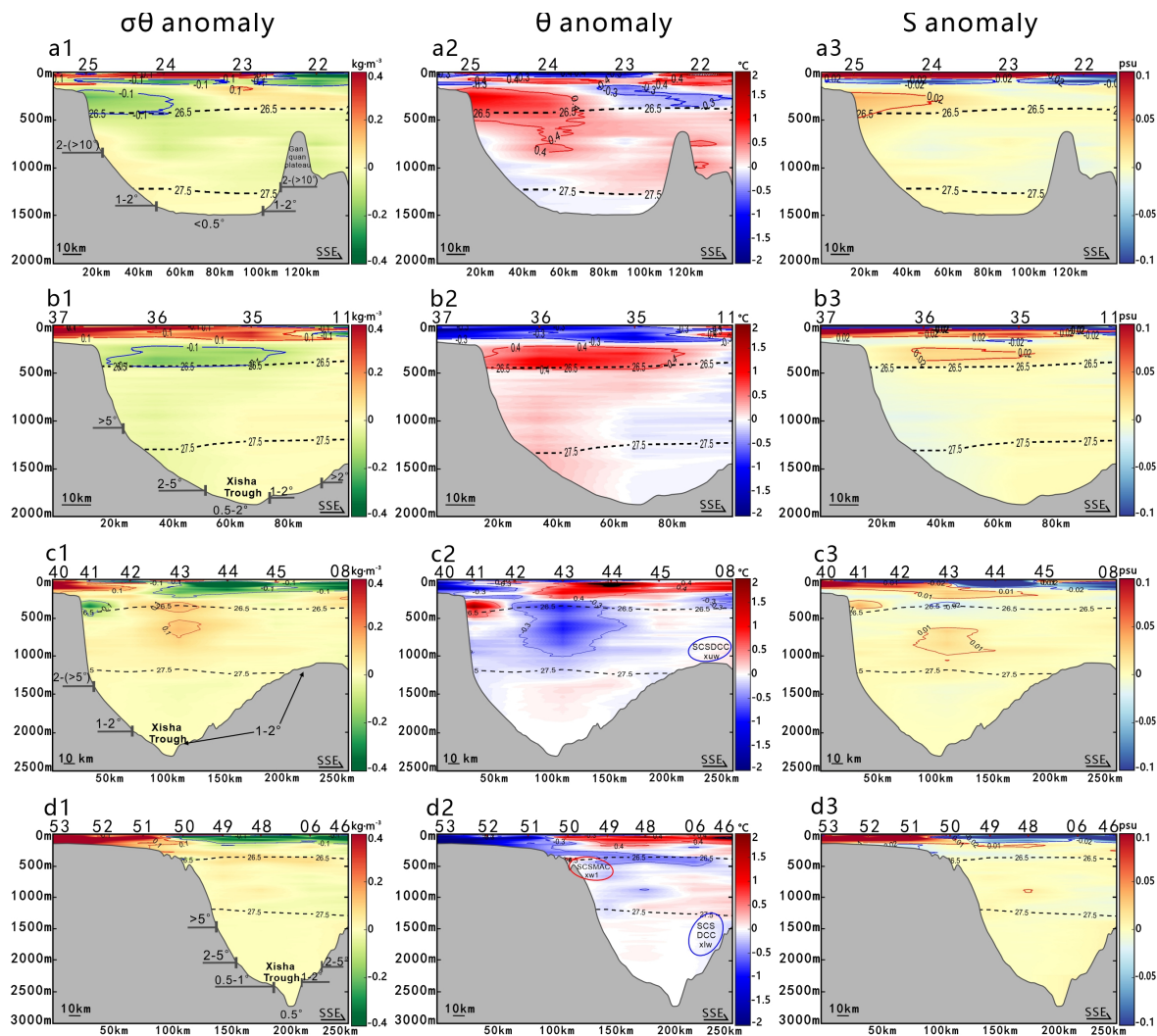


**Figure 7.** Profiles showing  $\sigma\theta$  anomaly (a1,b1,c1,d1),  $\theta$  anomaly (a2,b2,c2,d2), and  $S$  anomaly (a3,b3,c3,d3) and seabed morphologies. The red oval curves include  $\theta$  anomaly scope of SCSMACxw1. The blue oval curves indicate  $\theta$  anomaly scope of SCSDCCxuw and SCSDCCxlw. (a1,a2,a3) Profile from the upstream depression belt; (b1,b2,b3) Profiler from the mid-upper stream depression belt. (c1,c2,c3) Profiler from the midstream depression belt. (d1,d2,d3) Profiler from the mid-lower stream depression belt. Thick black dashed lines outline  $\sigma\theta = 26.5\text{--}27.5 \text{ kg}\cdot\text{m}^{-3}$ .

SCSMACxw2 has an eastward direction, passing through station 35 in profile (II), where its velocity exceeding 20 cm/s has a larger thickness (500–1500 m) than those of SCSMACxw in profile (I), with a vertical distribution of the  $\theta$  anomaly that is similar to SCSMACxw1 (Figures 5(a1), 6(b1) and 7(b2)). Flowing eastward, SCSMACxw2 reaches station 43 in profile (III) and then turns direction towards the northeast (Figure 5(a1)). Its velocity core deepens to 800–1600 m and extends to ~50 km wide, with a  $\theta$  anomaly of  $< -0.3 \text{ }^{\circ}\text{C}$  at 500–1100 m and  $\sim +0.1 \text{ }^{\circ}\text{C}$  below 1100 m (Figures 6(c1) and 7(c2)). At station 49 in profile (IV), the middle-layer anticyclonic circulation of SCS in the Yitong slope (SCSMACy) is observed flowing towards the northeast (Figures 5(a1) and 6(d1)). Its core velocity exceeds 20 cm/s with a negative  $\theta$  at a depth of 800–1500 m (Figures 6(d1) and 7(d2)).

The slope current (SC) flows southwestwards, passing through station 50 in profile (IV), station 41 in profile (III), as well as station 36 in profile (II) (Table S2). Specifically, SC is observed partially turning backward southeast through stations 41 and 36 in Figure 5(a1). SC has a velocity of  $>10\text{--}20 \text{ cm/s}$  in profiles (IV) and (III), where it is 100–600 m and 100–1000 m deep (interspersed with the SCSMACxw1), respectively (Figure 6(c1,d1)). In

profile (II), its velocity and width reduce to  $<15$  cm/s and to  $\sim 20$ – $30$  km at  $400$ – $600$  m, respectively (within the scope of SCSMACxw1) (Figure 6(b1)). Below  $500$  m,  $\theta$  anomaly of SC increases from a negative anomaly of  $<-0.3$  °C in profiles (III and IV) to a positive anomaly of  $<+0.4$  °C in profile (II) (Figure 7(b2,c2,d2)).

SCSDCCxuw is observed flowing northwestward at station 08 in profile (III), with a velocity of  $>10$  cm/s at depths between  $800$  and  $1300$  m, accompanied by a positive  $\theta$  anomaly of  $0$  to  $+0.1$  °C (Figures 6(c1) and 7(c2)). SCSDCCxlw is observed at station 46 in profile (IV). The upper  $800$ – $1500$  m of SCSDCCxlw flows northwards/northwestwards, with a velocity and  $\theta$  anomaly exceeding  $10$  cm/s and from  $-0.1$  to  $+0.1$  °C, respectively (Figures 5(a1,a2), 6(d1) and 7(d2)). Passing station 06, the lower  $1300$ – $2000$  m of SCSDCCxlw partially flows southwestwards, with a velocity of  $<10$  cm/s and a negative  $\theta$  anomaly (Figures 6(c1) and 7(c2)).

EC flows northeast passing through station 45 in profile (III). It has a velocity of  $>20$  cm/s at  $50$ – $400$  m, with a positive  $\theta$  anomaly (Figures 6(d1), 7(d2) and S1a,b). In addition, WCs flow southwest passing through station 06 in profile (IV), station 43 in profile (III), and 35 in profile (II), with a velocity of  $>20$  cm/s at  $0$ – $400$  m (Figures 6(b1,c1,d1) and S1a,b).

### 3.3. Modeling of Currents around the Central Depression Belt

Model results show that the middle layer currents ( $400$ – $1300$  m deep) in the central depression belt connect to the middle-layer anticyclonic circulation of SCS (SCSMAC) [19,46] (Figure 5(a2)), whereas the deep-layer currents ( $>1300$  m deep) link to the deep-layer cyclonic circulation of SCS (SCSDCC) [22–25,47] (Figure 5(b2)). SCSMAC flows northwards along the western continental margin of SCS, encountering the Qiongdongnan Basin and Xisha Uplift at the SCS northwestern corner. On the south side of the Xisha Uplift, SCSMAC bifurcates into two branches of SCSMACxe (as the eastern one) and SCSMACxw (as the western one, flowing north into the central cayon). The slope current (SC) ( $200$ – $1000$  m deep) [20,21,48] traveling from the northwest generates the southwestward SC at the northwest flank of the depression belt (Figure 5(a2)). SCSDCC flows southwards, crossing the Northwest Sub-Basin along the eastern side of the Xisha Uplift (Figure 5(b2)).

The climatological summer (MJJ) results from HYCOM reveal the features of currents in the horizontal and vertical distributions as follows (Figures 5(a2,b2), and 6(a2,b2,c2,d2)) and are listed (see Supplementary Table S3):

SCSMACxe flows eastwards with a velocity of  $\sim 1.5$ – $5$  cm/s at  $600$ – $1400$  m along the Xisha Uplift southern flank, which turns northward at the southeast of Xisha Uplift (Figure S3(a1)). Passing through the channel between the Zhongjian Terrace and Xisha Uplift (around station 19), SCSMACxw, with a velocity of  $>5$  cm/s at  $400$ – $1000$  m, flows northwestwards into the central depression belt and reaches station 16 (Figure 5(a2)). On the NW flank of the upstream depression belt, SCSMACxw has a velocity of  $\sim 5$ – $10$  cm/s at a depth of  $500$ – $1000$  m and turns its direction northeast. It flows along the depression belt's NW flank to the mid-upper stream (around stations 12 and 35), where it maintains velocity but bifurcates into a western branch (SCSMACxw1) and an eastern branch (SCSMACxw2). Along the SE flank of the upstream depression belt, the reversed branch SCSMACxw flows southwestwards (stations 30, 31, and 22), developing as SCSMACxw3 with a velocity of  $\sim 1$ – $3$  cm/s. In further, SCSMACxw1 and SCSMACxw3 jointly develop a local anticyclonic circulation in the upstream depression belt (Figure 5(a2.1)).

SCSMACxw1 keeps flowing northeastward to station 36 in profile (II) and reaches station 41 in profile (III) along the NW flank of the midstream depression belt, with a velocity of  $\sim 1$ – $4$  cm/s at a  $500$ – $1400$  m depth (Figure 6(b2,c2)).

SCSMACxw2 turns eastwards at stations 35 and 11 in profile (II) and across the depression belt, whereas its mainstream with a velocity of  $\sim 1$ – $3$  cm/s at  $500$ – $1000$  m passes through station 45 in profile (III) along the depression belt's SE flank (Figures 5(a2.1) and 6(b2,c2)).

The southwestward SC enters the NW flank of the depression belt through the Yitong slope (Figure 5(a2.1)). Passing by stations 49 and 50 in profile (IV), SC has a velocity of  $\sim 5$ – $20$  cm at a depth of  $0$ – $600$  m and encounters SCSMACxw1, with the interface occurring



at ~500–600 m (Figure 6(d2)). From the midstream to upstream, the velocity and scope of SC decrease from ~5–15 cm/s at 0–500 m in profile (III) to ~0.5 cm/s at 100–200 m in profile (I) (Figure 6(a2,b2,c2)).

The southward-flowing SCSDCC bifurcates at the eastern flank of Yongxing Island (Figure 5(b2.1)). The mainstream branch of SCSDCC (1300–2500 m deep) continues processing towards the east flank of Xisha Uplift in the south. The rest of the currents turn southwestwards, as SCSDCC<sub>xw</sub>, with a velocity of ~1–1.5 cm/s at 1000–2500 m (Figures 5(b2.1) and S3(b1,c1)). On its way through the southern margins of Yongxing Island and Zhaoshu Plateau, SCSDCC<sub>xw</sub> encounters the north-flowing SCSMAC<sub>xe</sub> and develops into a northwestward-flowing SCSDCC<sub>xuw</sub> and a northward SCSDCC<sub>xlw</sub> (Figures 5(a2.1,b2.1) and S3(d1,e1)).

SCSDCC<sub>xuw</sub> has a velocity of ~1–2 cm/s at a depth of 1000–1500 m and passes through the southwestern flank of the Zhaoshu plateau and enters northwestwards into the midstream depression belt (around stations 07, 08). SCSDCC<sub>xlw</sub>, at a depth of 1000–2000 m, initially flows northwards between Zhaoshu Plateau and Yongxing Island, then partially deflects westwards and continues flowing along the northern margin of Zhaoshu Plateau (between stations 47/06 and 46) (Figures 5(b2.1) and S3(e1)).

Note that, when SCSMAC<sub>xw2</sub> flows northeast along the SE flank of the mid-downstream depression belt, it encounters first with the northwestward SCSDCC<sub>xuw</sub> around stations 44 and 45 in profile (III) and then with SCSDCC<sub>xlw</sub> around station 06 in profile (IV). Then, their currents flow northwards, crossing the downstream depression belt, and encounter the northeast-flowing SCSMAC<sub>xw1</sub> and develop a merger flow of SCSMAC<sub>y</sub>. Around stations 48 and 49 in profile (IV) and station 05, SCSMAC<sub>y</sub> has a velocity of ~5 cm/s at 800–1500 m, flowing eastward along the Yitong slope (Figures 5(b2.1) and 6(d2)). In further, the westwards SCSDCC<sub>xlw</sub> flows along the SE flank of the mid-lower stream (station 06 in profile (IV)) and passes through the midstream (station 44 in profile (III)), where it has a velocity of ~1–4 cm/s (Figure 6(c2,d2)). Reaching the mid-upper stream (station 11 in profile (II)), its velocity decreases to 0–2 cm/s (Figures 5(b2.1) and 6(b2)).

The upper EC flows northeastward, passing through stations 07, 08, 45, and 46, sweeping along the Xisha Uplift, Zhaoshu Plateau, and Yongxing Island from west to east. It has a velocity of ~5–25 cm/s at depths of 0–300 m (Figures 6(c2,d2) and S1c).

### 3.4. Horizontal and Vertical Distributions of Turbulence Parameterizations in the Central Depression Belt

The layer-averaged dissipation rate ( $\epsilon_{MG}$ ) and diapycnal diffusivity ( $K_\rho$ ) are calculated to study the horizontal distributions of turbulence.

Figure 8 reveals that the dissipation rate changes with depth, with the magnitude of  $\epsilon_{MG}$  ranging from  $10^{-10}$  to  $10^{-9}$  W/kg. In the upper layer (50 to 400 m), the layer-averaged dissipation rate ( $\epsilon_{MGup}$ ) of the upstream depression belt is approximately  $1.2 \times 10^{-9}$  W/kg. The  $\epsilon_{MGup}$  of the mid-downstream depression belt is approximately  $2.5 \times 10^{-9}$  W/kg (Figure 7a). In the middle layer (400 to 1300 m), the layer-averaged dissipation rate ( $\epsilon_{MGmid}$ ) of the middle stream depression belt is approximately  $7 \times 10^{-10}$  W/kg. Areas with relatively high dissipation rates are at the depression belt's NW and SE flank of the mid-downstream, where dissipation rates are approximately  $5 \times 10^{-10}$  W/kg (Figure 8b). A similar spatial pattern of dissipation rates in the deep layer ( $\epsilon_{MGdeep}$ ; >1300 m to 500 m above the bottom) was observed, with an  $\epsilon_{MGdeep}$  of approximately  $2.5 \times 10^{-10}$  W/kg (Figure 8c). In the bottom layer (within 500 m above the bottom), the layer-averaged dissipation rate ( $\epsilon_{MGbot}$ ) of the upstream depression belt is approximately  $3 \times 10^{-10}$  W/kg, while that of the mid-downstream depression belt is weak, except for the slope on the depression belt's NW and SE flank, with a value of  $\sim 1.2 \times 10^{-10}$  W/kg (Figure 8d). The average dissipation rate of the different layers is shown in Figure 8e to evaluate the different regions of the depression belt, including the NW flank, SE flank, and central area. The average dissipation rate in the upper layer of the depression belt's NW flank, SE flank, and central area is one order of magnitude larger than those in the middle layer, deep layer,

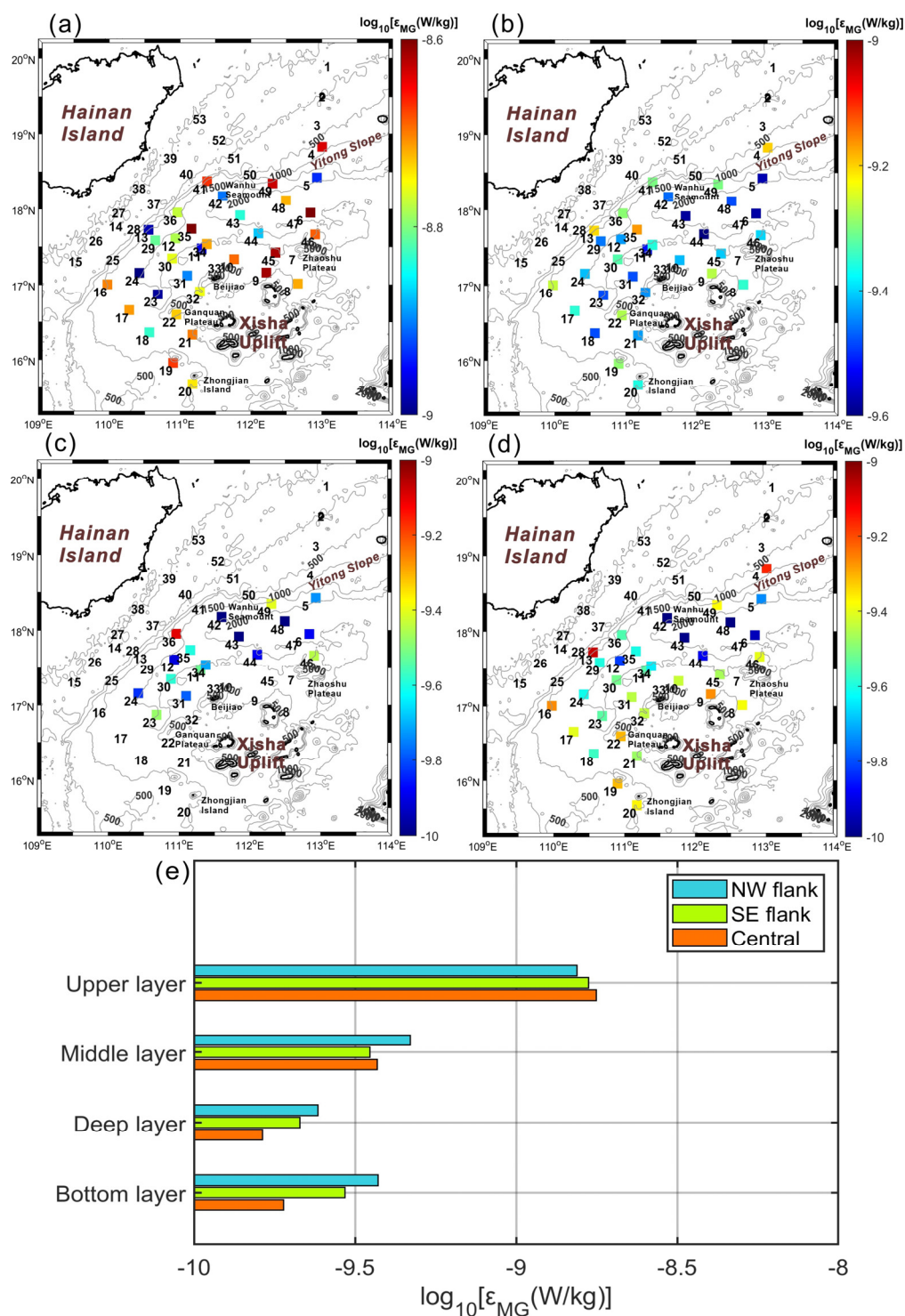
and bottom layers, with dissipation exceeding  $10^{-9}$  W/kg. The dissipation rate in the middle layer, deep, and bottom layers of the depression belt's NW flank is relatively high compared with those in the depression belt's SE flank and central area.

Figure 9 reveals variations in diapycnal diffusivity with depth, with a magnitude of  $K_\rho$  ranging from  $10^{-6}$  to  $10^{-5}$  m<sup>2</sup>/s. In the upper layer, the layer-averaged diapycnal diffusivity ( $K_{\rho up}$ ) of the upstream depression belt is  $10^{-6}$  m<sup>2</sup>/s. The  $K_{\rho up}$  reaches  $10^{-5}$  m<sup>2</sup>/s in the midstream depression belt (Figure 9a). In the middle layer, the layer-averaged diapycnal diffusivity ( $K_{\rho mid}$ ) is larger than  $K_{\rho up}$ . Elevated diffusivity in the midstream depression belt exceeds  $10^{-5}$  m<sup>2</sup>/s. An area with relatively high diffusivity is located along the depression belt's NW flank of the downstream, where diffusivity increases to  $10^{-5}$  m<sup>2</sup>/s (Figure 9b). In the deep layer, the layer-averaged diapycnal diffusivity ( $K_{\rho deep}$ ) is significantly increased and larger than in the middle layer. The mid-downstream of the depression belt is characterized by enhanced diffusivity exceeding  $10^{-5}$  m<sup>2</sup>/s (Figure 9c). In the bottom layer, the layer-averaged diapycnal diffusivity ( $K_{\rho bot}$ ) is elevated near the seamounts and Yitong slope, with values of  $10^{-5}$  m<sup>2</sup>/s (Figure 9d). The average diffusivity of different layers is shown in Figure 9e to evaluate the different regions of the depression belt. The diffusivity in the upper and middle layers of the depression belt's NW flank, SE flank, and central area have values of  $10^{-6}$  m<sup>2</sup>/s. Enhanced diffusivity is observed in the deep and bottom layers of the depression belt's different regions, with diffusivity exceeding  $10^{-5}$  m<sup>2</sup>/s. The diffusivity in the deep layer is relatively high compared with those in the bottom layer. In addition, the diffusivity in the bottom layers of the depression belt's central area is slightly larger than that in the depression belt's NW flank and SE flank (Figure 9e).

The  $\varepsilon_{MGup}$  is higher than  $\varepsilon_{MGmid}$ ,  $\varepsilon_{MGdeep}$ , and  $\varepsilon_{MGbot}$ , with an average value of  $2.5 \times 10^{-9}$  W/kg. The average values of  $\varepsilon_{MGdeep}$  and  $\varepsilon_{MGbot}$  are  $\sim 2.5\text{--}3.9 \times 10^{-10}$  W/kg (Figure 10a). The  $K_{\rho deep}$  and  $K_{\rho bot}$  are  $\sim 1\text{--}1.5 \times 10^{-5}$  m<sup>2</sup>/s, which are larger than the  $K_{\rho up}$  and  $K_{\rho mid}$  values of  $\sim 5.6\text{--}6.3 \times 10^{-6}$  m<sup>2</sup>/s (Figure 10b). The  $N^2$  exists in the upper, middle, deep, and bottom layers, with averaged values of  $8 \times 10^{-5}$  s<sup>-2</sup>,  $1.2 \times 10^{-5}$  s<sup>-2</sup>,  $2.8 \times 10^{-6}$  s<sup>-2</sup>, and  $3.9 \times 10^{-6}$  s<sup>-2</sup> (Figure 10c). The average  $S^2$  exists in the upper, middle, deep, and bottom layers, with averaged values of  $5 \times 10^{-6}$  m<sup>2</sup>/s,  $1 \times 10^{-6}$  m<sup>2</sup>/s,  $1.4 \times 10^{-6}$  m<sup>2</sup>/s, and  $1 \times 10^{-6}$  m<sup>2</sup>/s (Figure 10d).

On the NW flank of the mid-downstream depression belt, turbulence was relatively active at 300–1000 m in the middle layer (stations 36, 41, and 50), with the maximum dissipation rate reaching  $10^{-8}$  W/kg and the maximum diapycnal diffusivity exceeding  $10^{-4}$  m<sup>2</sup>/s (Figure 10a,b). Additionally, weak stratification and strong shear are observed (Figure 10c,d), leading to most of the water column in this region being characterized by  $Ri$  between 0.25 and 1, even  $Ri < 0.25$  at 300–500 m (Figure 11a). On the SE flank of the mid-downstream depression belt, turbulence was relatively active at 800–1500 m (stations 09, 44, 45, and 46), with the elevated dissipation rate ( $>10^{-9}$  W/kg) and diffusivity ( $>10^{-5}$  m<sup>2</sup>/s) (Figure 10a,b). In addition, the enhanced shear and  $Ri$  between 0.25 and 1 were observed in this region (Figure 11a).

In the center of the mid-downstream depression belt, however, the shear variance exceeds the buoyancy frequency below 1000–1300 m (stations 06, 35, 43, and 48), pushing  $Ri$  below 0.5 (even  $< 0.25$ ) in most of the water column (Figure 11a). The dissipation rate at corresponding depths was enhanced, with the diffusivity reaching  $10^{-4}$  m<sup>2</sup>/s (Figures 9b and 10a). Turbulence was more activated in the bottom and topographic obstacles (stations 07, 11, 19, 34, 42, and 49), with the high diffusivity exceeding  $10^{-4}$  m<sup>2</sup>/s (Figure 10b). The near-bottom  $Ri$  values vertically reduce to 0.5, even  $< 0.25$  (Figure 11a).



**Figure 8.** Maps of the layer-averaged dissipation rate ( $\epsilon_{MG}$ ) for the upper layer (a), middle layer (b), deep layer (c), and bottom layer (d). (e) Comparison of averaged dissipation rate ( $\epsilon_{MG}$ ) for the depression belt's different regions in each layer.



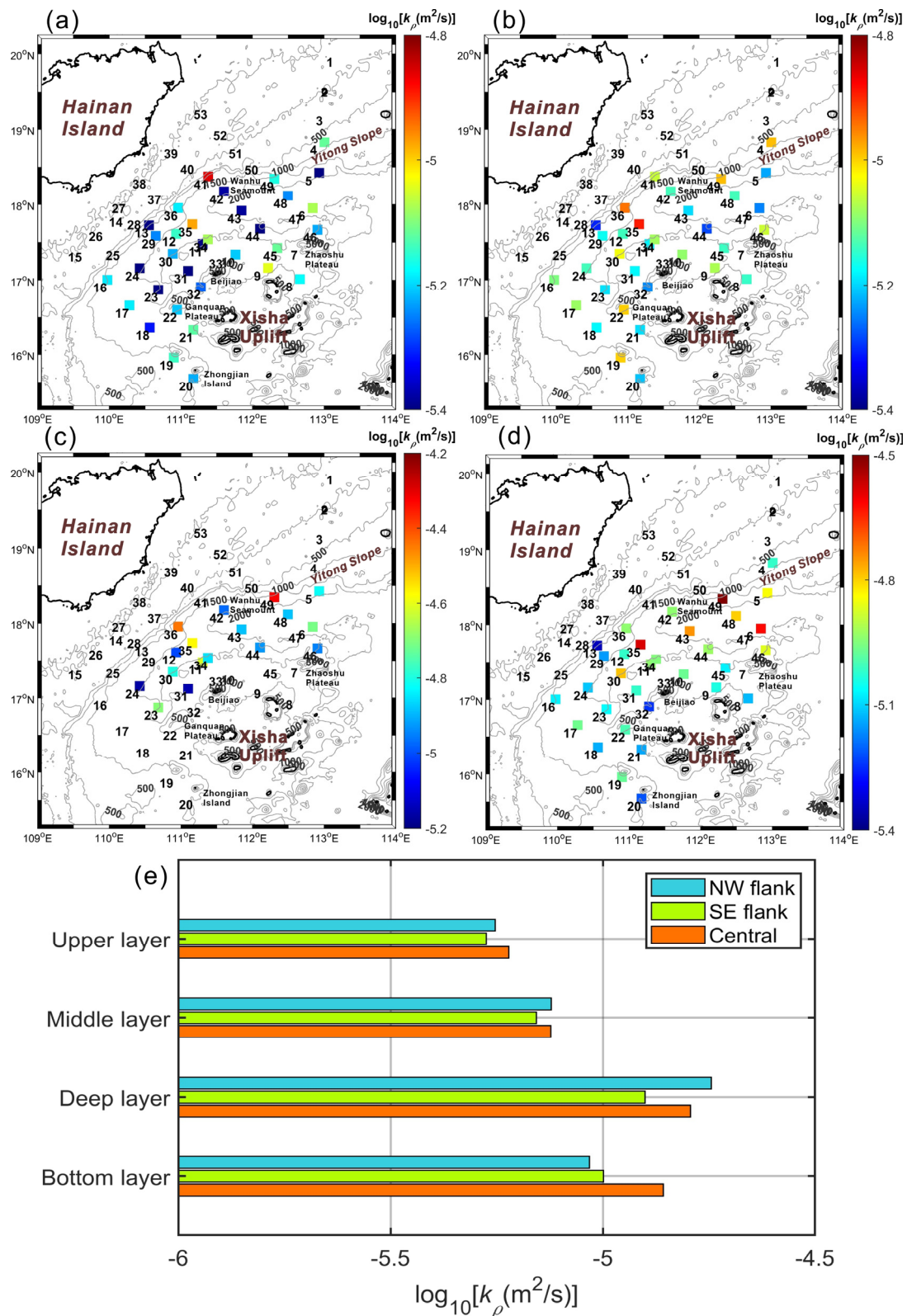


**Figure 9.** Maps of the layer-averaged diapycnal diffusivity ( $K_\rho$ ) for the upper layer (a), middle layer (b), deep layer (c), and bottom layer (d). (e) Comparison of averaged diapycnal diffusivity ( $K_\rho$ ) for the depression belt's different regions in each layer.

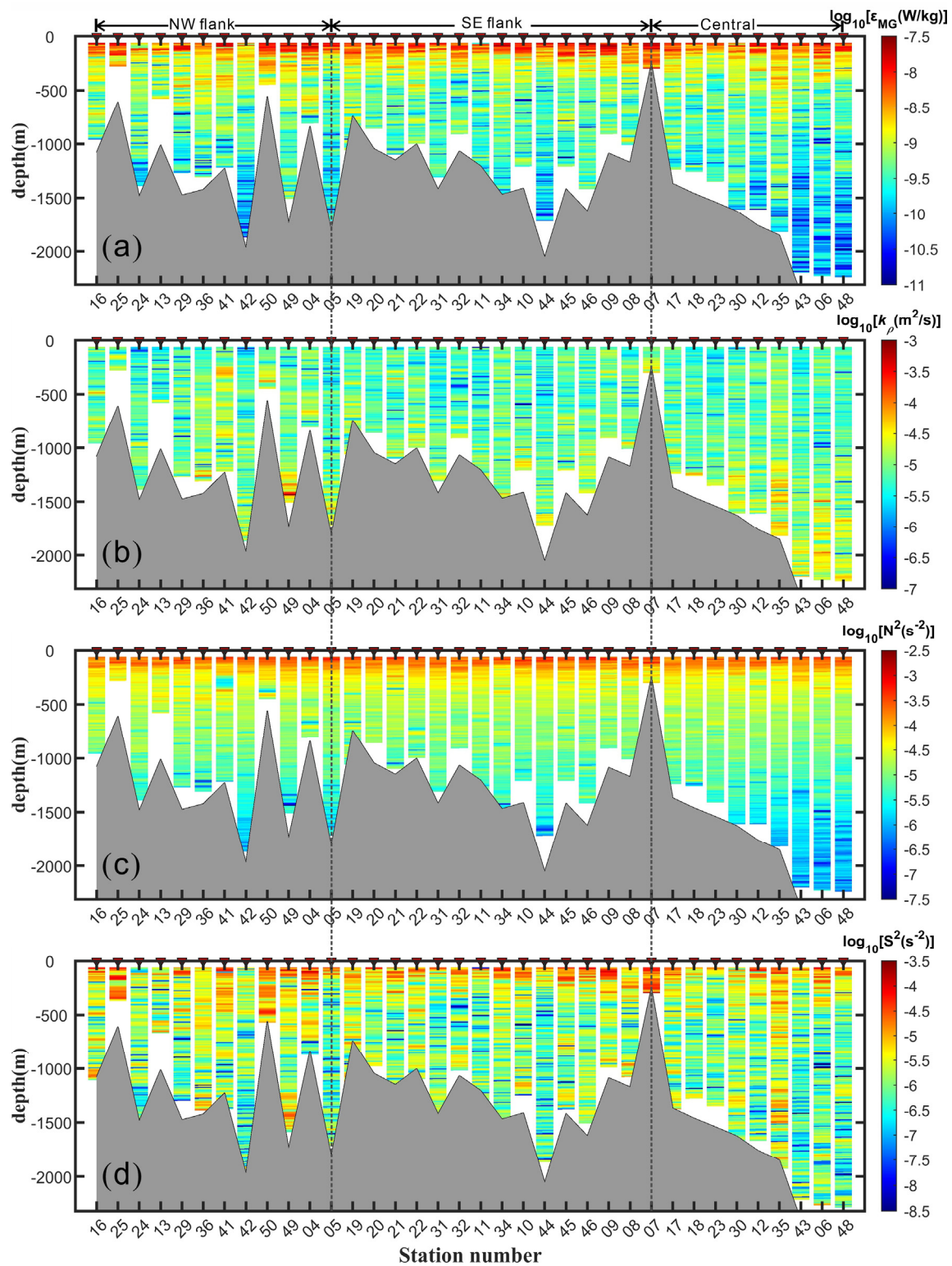


**Figure 10.** (a) Dissipation rate ( $\epsilon_{MG}$ ). (b) Diapycnal diffusivity ( $K_\rho$ ). (c) Buoyancy frequency squared ( $N^2$ ). (d) Shear variance ( $S^2$ ). Gray shading indicates the bathymetry. The vertical dashed lines divide the stations into three regions representing the depression belt's NW flank, the depression belt's SE flank, and the depression belt's central area, respectively.

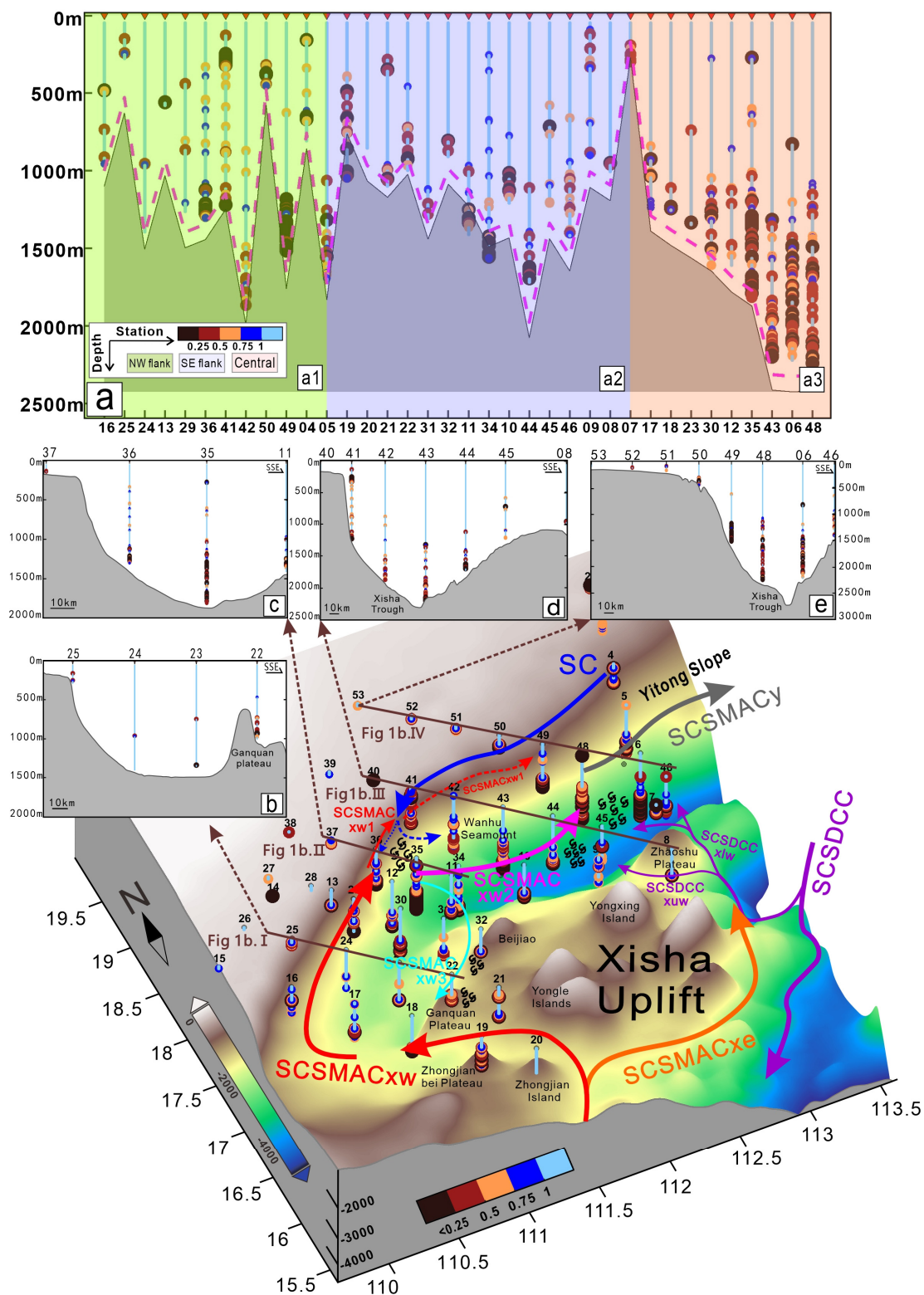


**Figure 11.** Spatial distribution of Richardson number. The orange arrow represents SCSMACxe. The red arrows include SCSMACxw and SCSMACxw1. The magenta arrow indicates SCSMACxw2. The gray arrow is SCSMACy. The cyan arrow indicates SCSMACxw3. The blue arrows represent SC. The purple arrows include SCSDCC, SCSDCCxuw, and SCSDCCxlw. The black arrows represent the enhanced local mixing. (a) Three regions divided the central depression belt's NW flank (a1), SE flank (a2), and central area (a3), respectively. The magenta dashed line indicates ~100 m above the bottom. (b–e)  $Ri$  in Profile I, II, III, and IV, respectively.



## 4. Discussion

### 4.1. Mid-Deep Circulation Pattern in the Central Depression Belt

The observation and model results of the circulation pattern in the central depression belt show that (i) SCSMACxw flows northeastwards along the NW flank of the upstream central depression belt and bifurcates into the SCSMACxw1 and SCSMACxw2, reversing to form the southwestward-flowing SCSMACxw3; (ii) the northwestward-flowing SCSMACxw1 meets head-on with the southwestward-flowing SC on the NW flank of the midstream depression belt; (iii) SCSMACxw2 flows eastwards through the center of mid-upper stream depression belt; (iv) SCSDCCxuw flows northwestwards through the SE flank of midstream; SCSDCCxlw flows mainly northwards and deflects partially westwards on the SE flank of the mid-lower stream depression belt; (v) at the terminus of SCSMACxw2 and SCSMACxw1, SCSMACy flows northeastward at the NW flank of the mid-lower stream depression belt (Figures 5(a1,a2.1) and 12).

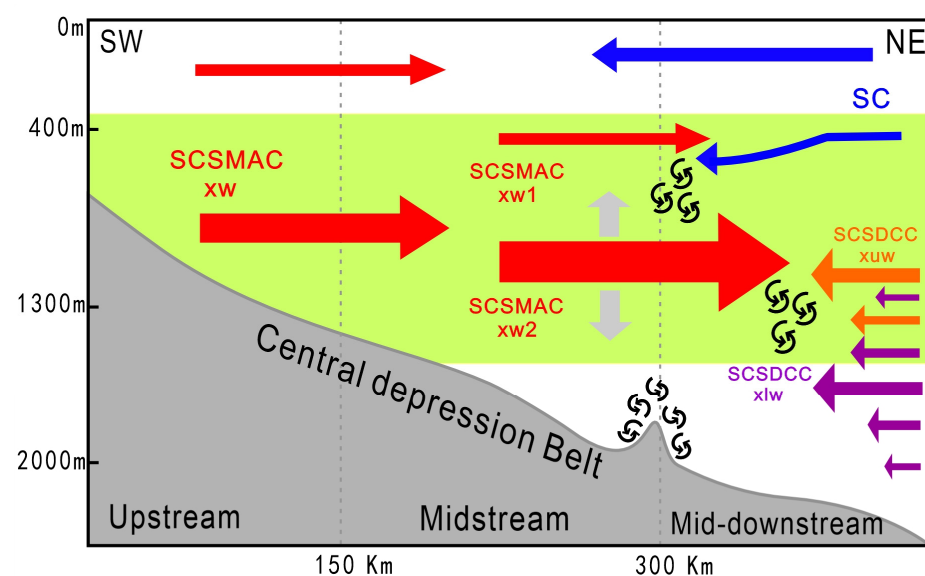


**Figure 12.** Schematic diagram of the vertical structure of summer circulation in the central depression belt. The red vectors are SCSMACxw, SCSMACxw1, and SCSMACxw2. The blue vectors are SC. The orange vectors are SCSDCCxuw. The purple vectors are SCSDCCxlw. The green area is middle layer depth. The gray area is seafloor topography.

#### 4.1.1. SCSMACxw1 Converges with SC at 300–1000 m

After converging, both the SCSMACxw1 and SC experience reduced speed along their original directions (Table S2). Meanwhile, SCSMACxw1 shrinks the positive  $\theta$  anomaly scope of  $>+0.4$  °C both in thickness (from 300–500 m at a depth of 500 m) and in width (from ~60 km wide to less than 10 km); SC shifts the initially high negative  $\theta$  anomaly to positive. The above demonstrates that SCSMACxw1 and SC interact strongly enough to significantly change their original properties. In the Mar del Plata submarine canyon on the Argentine margin, where the Malvinas Current converges with the Brazil Current at ~500–2000 m in depth, a similar situation occurs [49].

Observations reveal that SC enters the central depression belt from the northeast and sinks from an average depth of ~400 m in profile (VI) to ~600 m in profile (III), where its velocity core ( $>20$  cm/s, southwestward) converges with SCSMACxw1 ( $<20$  cm/s, northeastward). The model results further present that SCSMACxw1 and SC converge at an interface at ~500–600 m. Thus, observational and numerical data consistently show that this is a direct result of the converging interaction of SCSMACxw1 and SC (Figure 6c,d).

In profile (III), the core velocity and corresponding scope thickness/width of SC are apparently smaller in model results (5–15 cm/s, 0–500 m deep/~60 km wide) than those obtained from observations ( $>10$ –20 cm/s, 100–1000 m deep/~70 km wide). This indicates

that the vertical intensity of SC as well as the hydrodynamic enhancement over the northern flank of the central depression belt are underestimated by the model results. This may be partly due to the fact that the analysis is based on the climatological summer of the 20-year simulation average from May–July of 1993–2012, which smooths the seasonal variation of the currents such as the SC [48,50–53].

#### 4.1.2. SCSMACxw2 Converges with SCSDCCxuw and SCSDCCxlw at 1000–2000 m

Observations reveal that SCSMACxw2 flows eastward and reaches profile (III), where its core (800–1600 m deep) meets SCSDCCxuw (northwestward, 800–1300 m deep) at around stations 44 and 45. After converging, SCSMACxw2 has a northward core velocity of  $<20$  cm/s in profile (IV), where it meets SCSDCCxlw (northwards/westwards, 1000–2000 m deep) at around stations 06 and 46. The model results are synchronized in response to the interface between SCSMACxw2 and the westward SCSDCCxlw at a depth of 800–1300 m (Figure 6(b2,c2)). After converging, the westward SCSDCCxlw gradually weakens (reducing both velocity and scope) and the northward SCSMACxw2 catches up to the northeastward SCSMACxw1 (that has interacted with SC), which develops SCSMACy at a depth of 500–1500 m, around station 49 (Figure 5(a2.1)).

### 4.2. Factors Affecting the Central Depression Belt Circulation Pattern

#### 4.2.1. Local Wind and Eddies

During the observation period (i.e., summer), east winds prevail over the northwest edge of the SCS, the direction of which is opposite that of the summer monsoon (Figure S1a). Upper-surface layer currents in the central depression belt are dominated by the easterly/northeasterly wind [54] (Figure S1b), e.g., the west/southwest flowing WCs. Despite their fast velocities of  $>20$  cm/s, they are restricted to water depths above 500 m. Currents in the mid-deep layer at ~500–1500 m water depth flow predominantly in a northeasterly direction in the same region, such as SCSMACxw1 and SCSMACxw2, which have velocities exceeding 20 cm/s and directions opposite of WCs. Thus, local winds substantially affect upper currents, while mid-deep currents remain relatively untouched.

Based on sea-level anomalies (SLAs), our summer observations detected a warm eddy on the eastern flank of the Xisha Uplift (Figure S1a). This eddy is presented in the climatological summer HYCOM results as a weak anticyclonic circulation in the upper layers (see AC in Figure S1c). In the vicinity of stations 07, 08, 44, 45, and 46 around the Zhaoshu Plateau, EC are northeasterly, which is more consistent with the anticyclonic eddy flow tendency than with that of the easterly winds. In comparison, the upper (0–400 m deep) currents on the NW flank of the central depression belt prevail in the southwest direction, which may indicate limited influence from the eddy in this region (Figure S1b).

#### 4.2.2. Seabed Topography Changes

Topographic changes can modify the properties of mid-deep currents, such as shifting directions/scope depths and amplifying velocities and core fields. The location where SCSMACxw bifurcates and reverses in profile (II) belongs to the transition zone on the NW flank of the depression belt that connects its up- and midstream. Between profiles (I) and (II), the NW side steep slopes of  $>2^\circ$  are found only in 750–250 m water depths, while their depth range doubles in profile (II) (1700–200 m deep, specifically,  $>5^\circ$  in 1200–250 m depths) (Figure 3a,b). Meanwhile, the central depression belt tightens in width by half between both flanks of the 1000 m isobaths (from ~100 to ~50 km) (Figure 2; Table S1). On the other hand, the location where the southwestward SC sinks between profiles (VI) and (III) roughly divides the mid- and downstream depression belt (i.e., around the Wanhua Seamount) (Figure 1a). The NW flank of this depression belt generally has slopes from  $2^\circ$  to  $5^\circ$ , while, on the NW side of the Wanhua Seamount the slopes at 250/500–1500 m deep, they are  $>5^\circ$  (Figures 2c and 3c). We believe that such extensive increases in narrowness and steep slopes can directly induce shear instability, manipulating currents to meander and/or bifurcate [55–57].

In profile (II), the core velocity and corresponding scope thickness/width of SCSMACxw2 are less than half in the model results (1–3 cm/s, 600–1000 m deep) than those from observations (>20 cm/s, 500–1500 m deep); the velocity cores of SCSMACxw2 and SCSMACxw1 are located ~20 km closer to the SE flank of the central depression belt in the model results (Figure 5(b2)). In profile (III), from observations, SCSMACxw2 doubles the width and sinks ~200 m deep (Table S2), and the changed vertical structure is scarcely shown in the model results (Figure 6(c2)). The above demonstrates that SCSMACxw2 is significantly more intensified both horizontally and vertically in observations. The low-resolution bathymetry of 10 km in HYCOM smoothed out small-scale changes in topography, which would explain such differences in both the flow intensification and watershed between the HYCOM results and observations. Small-scale topographic changes within 10 km prevail all over the seamounts (e.g., the channel between Zhaoshu Plateau and Yongxing Island, numerous local mounds, or depressions), which are able to critically manipulate the intensity of energy radiation and the velocity/direction of mean currents [4,9,10,58], triggering baroclinic instability and inducing local eddies [59]. Their effects should be particularly pronounced in mountainous regions where the topography changes dramatically [17]. We believe a similar situation occurs for SCSMACy in profile (VI) (Figure 6(d2)), where the NW flank of the mid-downstream depression belt slope of the model topography is limited within 2° after the 10 km smoothing (Figure S4).

Although the direction of SCSMACxw2 is consistent with that of the surface eddy, there is a clear boundary between their velocity cores in profile (III). Relevant blocking may also come from the SE side seamounts (Figure 6(c1)). Thus, we suggest that it is the seabed topography that changes instead of local winds and mesoscale eddies that directly manipulate the development of local circulation patterns in the mid-deep central depression belt.

#### 4.3. Enhanced Mixing in the Central Depression Belt

The results indicate that turbulent mixing in the middle layer of the depression belt exhibits spatially non-uniformity. Enhanced mixing on the NW flank of the midstream depression belt (near stations 36 and 41) is more active than in other regions, with diffusivity exceeding  $10^{-5}$  m<sup>2</sup>/s (Figures 9b and 10b). The turbulent mixing shear variance and stratification made significant contributions. The elevated vertical shear was larger than stratification at the middle layer in this region (Figure 10c,d), where the intensification and bifurcation of SCSMACxw, and the convergence of SCSMACxw1 and SC, are evident (Figures 5a and 6). The low *Ri* (Figure 11a) implies that shear instability [30,60–62] occurs in these conditions and produces enhanced dissipation and diapycnal diffusivity. There are some factors in the region that can contribute to turbulent mixing, such as near-inertial internal waves and internal tides. The wind-forced, near-inertial waves are a small contribution to the turbulent mixing below the upper layer [63]. Alternatively, the steep slope and Wanhua seamount exist on the NW flank of the midstream depression belt (Figure S4b). Thus, local mixing is considered to be related to the breaking of internal tides over critical slopes [64], as well as the generation of lee waves trapped over the seamount [65,66].

Below 1000–1300 m, enhanced mixing occurs where the strengthened SCSMACxw2 converges with SCSDCCxuw and SCSDCCxlw in the central area of the mid-downstream depression belt away from the flank (stations 06, 43, 48) (Figure 5). The mixing level increases, with diffusivity exceeding the order of  $10^{-5}$  m<sup>2</sup>/s (Figures 9c and 10b), accompanied by low *Ri* (Figure 11a). These findings suggest that shear instability plays a relatively important role in driving local mixing at the mid-deep layer in this region.

In the bottom layer, elevated dissipation rate and diffusivity can be identified, with the maximum  $\epsilon_{MG}$  and  $K_\rho$  values exceeding  $10^{-9}$  W/kg and  $10^{-4}$  m<sup>2</sup>/s, respectively (Figures 8d,e and 9d,e). The dissipation rate on the NW and SE flank of the depression belt is higher than that in the center of the depression belt away from slope criticality (Figure 8e). High diapycnal diffusivity ( $\sim 10^{-3}$  m<sup>2</sup>/s) and very low *Ri* (<0.25) at station 49, near the bottom of the Yitong slope (Figures 9d and 11e), may be related to the breaking internal

tides and the intensified geostrophic shear. We believe enhanced mixing near the bottom should also be associated with deep eddies and topographic Rossby waves, besides the breaking internal tides [15–17,67]. The observations presented in this paper, however, fail to directly address these processes, which warrant intensive attention in future studies.

## 5. Conclusions

- (1) Observation and model results consistently reveal the mid-deep circulation structure in the central depression belt (Figures 11 and 12) as follows:

Directly derived from SCSMACxw, mid-deep currents named SCSMACxw1 and SCSMACxw2 in the central depression belt are highlighted in this article. Since entering the central depression belt from the most SW upstream, the mainstream currents of the northeastward SCSMACxw (average core depth = ~700 m) run along the NW flank of the upstream depression belt and bifurcates into the SCSMACxw1 and SCSMACxw2 in the mid-upper stream.

SCSMACxw1 (average core depth = ~500–600 m) converges with the southwestward-flowing SC (average core depth = 400–600 m) on the NW flank of the midstream depression belt and continues the NE movement.

SCSMACxw2 (average core depth = 1000–1200 m) turns eastwards first across the depression belt to the SE side of its midstream. Flowing northeast along the SE flank, the SCSMACxw2 converges with the flow (SCSDCCxuw and SCSDCCxlw, average core depth = 1000–1600 m). After converging, SCSMACxw2 turns northeastward and reunites with SCSMACxw1 at the NW side of the mid-lower stream depression belt, developing SCSMACy (average core depth = ~1000 m), which flows eastwards along the Yitong slope.

- (2) Over the central depression belt region, seabed topography changes have a decisive impact on developing a local mid-deep circulation pattern, where current intensification is promoted by current–topography interactions. In comparison, winds and mesoscale eddies can substantially affect upper-surface currents while having limited influence in the mid-deep layers.
- (3) Inconsistencies between model results and observations correspond to both the apparent lack of intensifications (i.e., velocities, core scopes) for SC and SCSMACxw2. The former is due to the fact that the model underestimates the seasonal variations in the strength and vertical structure of the slope currents along the northwestern margin of the SCS. The latter is because the topographic resolution used in the model (~10 km) is too low to capture the forcing signals of the real seabed topography in the mid-downstream.
- (4) Prominent convergence of SCSMACxw1 and SC from ~300 to 1000 m deep and of SCSMACxw2, SCSDCCxuw, and SCSDCCxlw from ~1000 to 2000 m deep significantly change the properties of the relevant currents and water masses (Figure 12). Enhanced local mixing is assigned to the relevant regions above, pointing out the convergence as a dominant mechanism for generating instability.

**Supplementary Materials:** The following supporting information can be downloaded at: <https://www.mdpi.com/article/10.3390/jmse12050700/s1>, Figure S1: SLA and depth-averaged velocity of LADCP, MJJ, and multi-year average in the upper (0–400 m); Figure S2: Depth-averaged velocity of multi-year average in the middle and deep layer; Figure S3: Vertical velocity of MJJ and multi-year average at different locations around the Xisha Uplift; Figure S4: Slope of HYCOM and GEBCO\_2023; Table S1: Seabed morphology characteristics of central depression belt in profilers; Table S2: Currents and water mass properties in the profiles of the central depression belt from observation; Table S3: Current properties of climatological summer and multi-year average in the profiles from HYCOM.

**Author Contributions:** H.M.: conceptualization, methodology, formal analysis, investigation, writing—original draft; D.W.: conceptualization, writing—review and editing, project administration, and funding acquisition; H.C.: conceptualization, supervision, writing—review and editing; C.Q.: investigation, formal analysis, writing—review and editing; H.X.: formal analysis, visualization, supervision; X.S.:



software, data curation; W.Z.: supervision, writing—review and editing. All authors have read and agreed to the published version of the manuscript.

**Funding:** This work was supported by the National Natural Science Foundation of China (Grant Nos. 92158204; 42130408; 42376011), the Project of Southern Marine Science and Engineering Guangdong Laboratory (Zhuhai) (Grant Nos. 311022002; SML2021SP30), the Guangdong Basic and Applied Basic Research Foundation (Grant No. 2023A1515010967), and the Guangdong Key Areas R & D Project (Grant No. 2023B1111050014).

**Institutional Review Board Statement:** Not applicable.

**Informed Consent Statement:** Not applicable.

**Data Availability Statement:** Data associated with this research are available and can be obtained by contacting the corresponding author upon reasonable request.

**Acknowledgments:** The cruise of South China Sea western boundary currents on board the R/V Zhong Shan Da Xue and the cruise team from Center of Ocean Expedition of Sun Yat-sen University, the Deep Blue Exploration Offshore Engineering Practice Cruise (No. SLSK-00202310), and the data supplied by the GEBCO\_2023, HYCOM GLBu0.08, WOA18, and CMEMS (Copernicus Marine Environment Monitoring Service) datasets are gratefully acknowledged. The authors would also like to thank the support from the Group of Air–Sea Interaction in the School of Marine Sciences at Sun Yat-Sen University and the comments from editors and reviewers for greatly improving this manuscript.

**Conflicts of Interest:** The authors declare no conflict of interest.

## References

1. Eiff, O.S.; Bonneton, P. Lee-wave breaking over obstacles in stratified flow. *Phys. Fluids* **2000**, *12*, 1073–1086. [\[CrossRef\]](#)
2. Wang, D.; Wang, Q.; Zhou, W.; Cai, S.; Li, L.; Hong, B. An analysis of the current deflection around Dongsha Islands in the northern South China Sea. *J. Geophys. Res. Oceans* **2013**, *118*, 490–501. [\[CrossRef\]](#)
3. Naveira Garabato, A.C.; Frajka-Williams, E.E.; Spingys, C.P.; Legg, S.; Polzin, K.L.; Forryan, A.; Abrahamsen, E.P.; Buckingham, C.E.; Griffies, S.M.; McPhail, S.D. Rapid mixing and exchange of deep-ocean waters in an abyssal boundary current. *Proc. Natl. Acad. Sci. USA* **2019**, *116*, 13233–13238. [\[CrossRef\]](#) [\[PubMed\]](#)
4. Kunze, E.; Smith, S.G.L. The role of small-scale topography in turbulent mixing of the global ocean. *Oceanography* **2004**, *17*, 55–64. [\[CrossRef\]](#)
5. Yan, X.; Kang, D.; Curchitser, E.N.; Pang, C. Energetics of Eddy-Mean Flow Interactions along the Western Boundary Currents in the North Pacific. *J. Phys. Oceanogr.* **2019**, *49*, 789–810. [\[CrossRef\]](#)
6. Liu, X.; Wang, D.-P.; Su, J.; Chen, D.; Lian, T.; Dong, C.; Liu, T. On the Vorticity Balance over Steep Slopes: Kuroshio Intrusions Northeast of Taiwan. *J. Phys. Oceanogr.* **2020**, *5*, 2089–2104. [\[CrossRef\]](#)
7. Qiu, C.; Mao, H.; Liu, H.; Xie, Q.; Yu, J.; Su, D.; Ouyang, J.; Lian, S. Deformation of a warm eddy in the northern South China Sea. *J. Geophys. Res. Oceans* **2019**, *124*, 5551–5564. [\[CrossRef\]](#)
8. Su, D.; Lin, P.; Mao, H.; Wu, J.; Liu, H.; Cui, Y.; Qiu, C. Features of slope intrusion mesoscale eddies in the northern South China Sea. *J. Geophys. Res. Oceans* **2020**, *125*, e2019JC015349. [\[CrossRef\]](#)
9. Vilela-Silva, F.; Silveira, I.C.A.; Napolitano, D.C.; Souza-Neto, P.W.M.; Biló, T.C.; Gangopadhyay, A. On the Deep Western Boundary Current Separation and Anticyclone Genesis off Northeast Brazil. *J. Geophys. Res. Oceans* **2023**, *128*, e2022JC019168. [\[CrossRef\]](#)
10. Lee, S.K.; Pelegri, J.L.; Kroll, J. Slope Control in Western Boundary Currents. *J. Phys. Oceanogr.* **2001**, *31*, 3349–3360. [\[CrossRef\]](#)
11. Stommel, H. The westward intensification of wind-driven ocean currents. *Eos Trans. Am. Geophys. Union* **1948**, *29*, 202–206.
12. Harris, P.T.; Macmillan-Lawler, M.; Rupp, J.; Baker, E.K. Geomorphology of the oceans. *Mar. Geol.* **2014**, *352*, 4–24. [\[CrossRef\]](#)
13. Wu, Z.; Li, J.; Jin, X.; Shang, J.; Jin, X.; Li, S. Distribution, features, and influence factors of the submarine topographic boundaries of the Okinawa Trough. *Sci. China Earth Sci.* **2014**, *57*, 1885–1896. [\[CrossRef\]](#)
14. Holland, W.R. Baroclinic and topographic influences on the transport in western boundary currents. *Geophys. Fluid Dyn.* **1973**, *4*, 187–210. [\[CrossRef\]](#)
15. Spall, M.A. Boundary Currents and Watermass Transformation in Marginal Seas. *J. Phys. Oceanogr.* **2017**, *34*, 1197–1213. [\[CrossRef\]](#)
16. Shu, Y.; Wang, J.; Xue, H.; Huang, R.X.; Chen, J.; Wang, D.; Wang, Q.; Xie, Q.; Wang, W. Deep-Current Intraseasonal Variability Interpreted as Topographic Rossby Waves and Deep Eddies in the Xisha Islands of the South China Sea. *J. Phys. Oceanogr.* **2022**, *52*, 1415–1430. [\[CrossRef\]](#)
17. Jiang, X.; Dong, C.; Ji, Y.; Wang, C.; Shu, Y.; Liu, L.; Ji, J. Influences of Deep-Water Seamounts on the Hydrodynamic Environment in the Northwestern Pacific Ocean. *J. Geophys. Res. Oceans* **2021**, *126*, e2021JC017396. [\[CrossRef\]](#)
18. Zeng, L.; Wang, D.; Chen, J.; Wang, W.; Chen, R. SCSPD14, a South China Sea physical oceanographic dataset derived from in situ measurements during 1919–2014. *Sci. Data* **2016**, *3*, 160029. [\[CrossRef\]](#) [\[PubMed\]](#)

19. Gan, J.; Liu, Z.; Hui, R.C. A Three-Layer Alternating Spinning Circulation in the South China Sea. *J. Phys. Oceanogr.* **2016**, *46*, 2309–2315. [\[CrossRef\]](#)
20. Su, J. Overview of the South China Sea circulation and its influence on the coastal physical oceanography outside the Pearl River Estuary. *Cont. Shelf Res.* **2004**, *24*, 1745–1760.
21. Yuan, Y.; Liao, G.; Yang, C. The Kuroshio near the Luzon Strait and circulation in the northern South China Sea during August and September 1994. *J. Oceanogr.* **2008**, *64*, 777–788. [\[CrossRef\]](#)
22. Cai, Z.; Gan, J. Dynamics of the cross-layer exchange for the layered circulation in the South China Sea. *J. Geophys. Res. Oceans* **2020**, *125*, e2020JC016131. [\[CrossRef\]](#)
23. Wang, G.; Xie, S.-P.; Qu, T.; Huang, R.-X. Deep South China Sea circulation. *Geophys. Res. Lett.* **2011**, *38*, L05601. [\[CrossRef\]](#)
24. Lan, J.; Wang, Y.; Cui, F.; Zhang, N. Seasonal variation in the South China Sea deep circulation. *J. Geophys. Res. Oceans* **2015**, *120*, 1682–1690. [\[CrossRef\]](#)
25. Zhou, M.; Wang, G.; Liu, W.; Chen, C. Variability of the Observed Deep Western Boundary Current in the South China Sea. *J. Phys. Oceanogr.* **2020**, *50*, 2953–2963. [\[CrossRef\]](#)
26. Visbeck, M. Deep velocity profiling using lowered Acoustic Doppler Current Profiler: Bottom track and inverse solutions. *J. Atmos. Ocean. Technol.* **2002**, *19*, 794–807. [\[CrossRef\]](#)
27. Egbert, G.D.; Erofeeva, S.Y. Efficient Inverse Modeling of Barotropic Ocean Tides. *J. Atmos. Ocean. Technol.* **2002**, *19*, 183–204. [\[CrossRef\]](#)
28. Chassignet, E.P.; Hulburt, H.E.; Smedstad, O.M.; Halliwell, G.R.; Hogan, P.J. The hycom (hybrid coordinate ocean model) data assimilative system. *J. Mar. Syst.* **2007**, *65*, 60–83. [\[CrossRef\]](#)
29. Smyth, W.D.; Carpenter, J.R. *Instability in Geophysical Flows*; Cambridge University Press: Cambridge, UK, 2019; pp. 53–73.
30. Miles, J.W. On the stability of heterogeneous shear flows. *J. Fluid Mech.* **1961**, *10*, 496–508. [\[CrossRef\]](#)
31. MacKinnon, J.A.; Gregg, M.C. Mixing on the late-summer New England shelf-Solibores, shear, and stratification. *J. Phys. Oceanogr.* **2003**, *33*, 1476–1492. [\[CrossRef\]](#)
32. Yang, Q.; Zhao, W.; Liang, X.; Tian, J. Three-Dimensional Distribution of Turbulent Mixing in the South China Sea. *J. Phys. Oceanogr.* **2016**, *46*, 769–788. [\[CrossRef\]](#)
33. Shang, X.D.; Liang, C.R.; Chen, G.Y. Spatial distribution of turbulent mixing in the upper ocean of the South China Sea. *Ocean Sci.* **2017**, *13*, 503–519. [\[CrossRef\]](#)
34. Liang, C.R.; Shang, X.D.; Qi, Y.F.; Chen, G.Y.; Yu, L.H. Assessment of fine-scale parameterizations at low latitudes of the North Pacific. *Sci. Rep.* **2018**, *8*, 10281. [\[CrossRef\]](#) [\[PubMed\]](#)
35. Osborn, T.R. Estimates of the Local Rate of Vertical Diffusion from Dissipation Measurements. *J. Phys. Oceanogr.* **1980**, *10*, 83–89. [\[CrossRef\]](#)
36. Oakey, N.S. Determination of the Rate of Dissipation of Turbulent Energy from Simultaneous Temperature and Velocity Shear Microstructure Measurements. *J. Phys. Oceanogr.* **1982**, *12*, 256–271. [\[CrossRef\]](#)
37. Cheng, C.; Jiang, T.; Kuang, Z.; Ren, J.; Liang, J.; Lai, H.; Xiong, P. Seismic characteristics and distributions of Quaternary mass transport deposits in the Qiongdongnan Basin, northern South China Sea. *Mar. Pet. Geol.* **2021**, *239*, 105118. [\[CrossRef\]](#)
38. Li, S.; Alves, T.M.; Li, W.; Wang, X.; Rebescio, M.; Li, J.; Zhao, F.; Yu, K.; Wu, S. Morphology and evolution of submarine canyons on the northwest South China Sea margin. *Mar. Geol.* **2022**, *443*, 106695. [\[CrossRef\]](#)
39. Zeng, F.C.; Wang, D.W.; Li, Z.G.; Wang, W.T.; Dai, X.M.; Sun, Y.; Lv, L.W.; Wang, W.W.; Zheng, Y.; Su, Z.Y.; et al. The discovery of an active fault in the Qiongdongnan Basin of the northern South China Sea. *Mar. Pet. Geol.* **2024**, *163*, 106777. [\[CrossRef\]](#)
40. Chen, H.; Zhang, W.; Xie, X.; Gao, Y.; Shan Liu, S.; Ren, J.; Wang, D.; Su, M. Linking oceanographic processes to contourite features: Numerical modelling of currents influencing a contourite depositional system on the northern South China Sea margin. *Mar. Geol.* **2022**, *444*, 106714. [\[CrossRef\]](#)
41. Chen, H.; Xie, X.; Zhang, W.; Shu, Y.; Wang, D.; Vandorpe, T.; Van Rooij, D. Deep-water sedimentary systems and their relationship with bottom currents at the intersection of Xisha Trough and Northwest Sub-Basin, South China Sea. *Mar. Geol.* **2016**, *378*, 101–113. [\[CrossRef\]](#)
42. Yin, S.; Hernández-Molina, F.J.; Lin, L.; Chen, J.; Ding, W.; Li, J. Isolation of the South China Sea from the North Pacific Subtropical Gyre since the latest Miocene due to formation of the Luzon Strait. *Sci. Rep.* **2021**, *11*, 1562. [\[CrossRef\]](#) [\[PubMed\]](#)
43. Yin, S.; Hernández-Molina, F.J.; Lin, L.; He, M.; Gao, J.; Li, J. Plate convergence controls long-term full-depth circulation of the South China Sea. *Mar. Geol.* **2023**, *459*, 107050. [\[CrossRef\]](#)
44. Tian, J.; Yang, Q.; Liang, X.; Xie, L.; Hu, D.; Wang, F.; Qu, T. Observation of Luzon Strait transport. *Geophys. Res. Lett.* **2006**, *33*, L19607. [\[CrossRef\]](#)
45. Zhu, Y.; Sun, J.; Wang, Y.; Wei, Z.; Yang, D.; Qu, T. Effect of potential vorticity flux on the circulation in the South China Sea. *J. Geophys. Res. Oceans* **2017**, *122*, 6454–6469. [\[CrossRef\]](#)
46. Wang, D.; Wang, Q.; Cai, S.; Shang, X.; Yang, Q. Advances in research of the mid-deep South China Sea circulation. *Sci. China Earth Sci.* **2019**, *62*, 152–164. [\[CrossRef\]](#)
47. Qu, T.; Giron, J.B.; Whitehead, J.A. Deepwater overflow through Luzon Strait. *J. Geophys. Res. Atmos.* **2006**, *111*, C01002. [\[CrossRef\]](#)
48. Qu, T.; Mitsudera, H.; Yamagata, T. Intrusion of the North Pacific waters into the South China Sea. *J. Geophys. Res. Oceans* **2000**, *105*, 6415–6424. [\[CrossRef\]](#)

49. Wilckens, H.; Miramontes, E.; Schwenk, T.; Artana, C.; Zhang, W.; Piola, A.R.; Baques, M.; Provost, C.; Hernández-Molina, F.J.; Felgendreher, M.; et al. The erosive power of the Malvinas Current: Influence of bottom currents on morpho-sedimentary features along the northern Argentine margin (SW Atlantic Ocean). *Mar. Geol.* **2021**, *439*, 106539. [\[CrossRef\]](#)
50. Qu, T.; Lukas, R. The Bifurcation of the North Equatorial Current in the Pacific. *J. Phys. Oceanogr.* **2003**, *33*, 5–18. [\[CrossRef\]](#)
51. Qu, T.; Song, Y.T.; Yamagata, T. An introduction to the South China Sea throughflow: Its dynamics, variability, and application for climate. *Dyn. Atmos. Oceans* **2009**, *47*, 3–14. [\[CrossRef\]](#)
52. Nan, F.; Xue, H.; Yu, F. Kuroshio intrusion into the South China Sea: A review. *Prog. Oceanogr.* **2015**, *137*, 314–333. [\[CrossRef\]](#)
53. Zhong, Y.; Zhou, M.; Wanek, J.J.; Zhou, L.; Zhang, Z. Seasonal Variation of the Surface Kuroshio Intrusion into the South China Sea Evidenced by Satellite Geostrophic Streamlines. *J. Phys. Oceanogr.* **2021**, *51*, 2705–2718. [\[CrossRef\]](#)
54. Sverdrup, H.U. Wind-Driven Currents in a Baroclinic Ocean; with Application to the Equatorial Currents of the Eastern Pacific. *Proc. Natl. Acad. Sci. USA* **1947**, *33*, 318–326. [\[CrossRef\]](#)
55. Orlanski, I. The Influence of Bottom Topography on the Stability of Jets in a Baroclinic Fluid. *J. Atmos. Sci.* **1969**, *26*, 1216–1232. [\[CrossRef\]](#)
56. Susanto, R.D.; Gordon, A.L. Velocity and transport of the Makassar Strait throughflow. *J. Geophys. Res. Oceans* **2005**, *110*, C01005. [\[CrossRef\]](#)
57. Chen, C.; Kamenkovich, I. Effects of Topography on Baroclinic Instability. *J. Phys. Oceanogr.* **2013**, *43*, 790–804. [\[CrossRef\]](#)
58. Xie, J.; He, Y.; Cai, S. Bumpy Topographic Effects on the Transbasin Evolution of Large-Amplitude Internal Solitary Wave in the Northern South China Sea. *J. Geophys. Res. Oceans* **2019**, *124*, 4677–4695. [\[CrossRef\]](#)
59. Qiu, B.; Chen, S. Seasonal Modulations in the Eddy Field of the South Pacific Ocean. *J. Phys. Oceanogr.* **2004**, *34*, 1515–1527. [\[CrossRef\]](#)
60. Polzin, K.; Toole, J.; Ledwell, J.; Schmitt, R. Spatial Variability of Turbulent Mixing in the Abyssal Ocean. *Science* **1997**, *276*, 93–96. [\[CrossRef\]](#)
61. Abarbanel, H.D.; Holm, D.D.; Marsden, J.E.; Ratiu, T. Richardson number criterion for the nonlinear stability of three-dimensional stratified flow. *Phys. Rev. Lett.* **1984**, *52*, 2352. [\[CrossRef\]](#)
62. Canuto, V.M.; Howard, A.; Cheng, Y.; Dubovikov, M.S. Ocean Turbulence. Part I: One-Point Closure Model-Momentum and Heat Vertical Diffusivities. *J. Phys. Oceanogr.* **2001**, *31*, 1413–1426. [\[CrossRef\]](#)
63. Alford, M.H.; Cronin, M.F.; Klymak, J.M. Annual Cycle and Depth Penetration of Wind-Generated Near-Inertial Internal Waves at Ocean Station Papa in the Northeast Pacific. *J. Phys. Oceanogr.* **2012**, *42*, 889–909. [\[CrossRef\]](#)
64. Klymak, J.M.; Alford, M.H.; Pinkel, R.; Lien, R.; Yang, Y.J.; Tang, T. The Breaking and Scattering of the Internal Tide on a Continental Slope. *J. Phys. Oceanogr.* **2011**, *41*, 926–945. [\[CrossRef\]](#)
65. Carter, G.S.; Gregg, M.C.; Merrifield, M.A. Flow and Mixing around a Small Seamount on Kaena Ridge, Hawaii. *J. Phys. Oceanogr.* **2006**, *36*, 1036–1052. [\[CrossRef\]](#)
66. Nikurashin, M.; Ferrari, R. Global energy conversion rate from geostrophic flows into internal lee waves in the deep ocean. *Geophys. Res. Lett.* **2011**, *38*, L08610. [\[CrossRef\]](#)
67. Gula, J.; Molemaker, M.J.; McWilliams, J.C. Topographic generation of submesoscale centrifugal instability and energy dissipation. *Nat. Commun.* **2016**, *7*, 12811. [\[CrossRef\]](#)

**Disclaimer/Publisher’s Note:** The statements, opinions and data contained in all publications are solely those of the individual author(s) and contributor(s) and not of MDPI and/or the editor(s). MDPI and/or the editor(s) disclaim responsibility for any injury to people or property resulting from any ideas, methods, instructions or products referred to in the content.